Massive Stars in the Arches Cluster [12]

Donald F. Figer[3,4], Francisco Najarro[5], Diane Gilmore[3],
Mark Morris[6], Sungsoo S. Kim[6], Eugene Serabyn[7],
Ian S. McLean[6], Andrea M. Gilbert[8], James R. Graham[8],
James E. Larkin[6], N. A. Levenson[4], Harry I. Teplitz[9,10]

ABSTRACT

[3]Space Telescope Science Institute, 3700 San Martin Drive, Baltimore, MD 21218; figer@stsci.edu

[4]Department of Physics and Astronomy, Johns Hopkins University, Baltimore, MD 21218

[5]Instituto de Estructura de la Materia, CSIC, Serrano 121, 29006 Madrid, Spain

[6]Department of Physics and Astronomy, University of California, Los Angeles, Division of Astronomy, Los Angeles, CA, 90095-1562

[7]Caltech, 320-47, Pasadena, CA 91125; eserabyn@huey.jpl.nasa.gov

[8]Department of Astronomy, University of California, Berkeley, 601 Campbell Hall, Berkeley, CA, 94720-3411

[9]Laboratory for Astronomy and Solar Physics, Code 681, Goddard Space Flight Center, Greenbelt MD 20771

[10]NOAO Research Associate

We present and use new spectra and narrow-band images, along with previously published broad-band images, of stars in the Arches cluster to extract photometry, astrometry, equivalent width, and velocity information. The data are interpreted with a wind/atmosphere code to determine stellar temperatures, luminosities, mass-loss rates, and abundances. We have doubled the number of known emission-line stars, and we have also made the first spectroscopic identification of the main sequence for any population in the Galactic Center. We conclude that the most massive stars are bona-fide Wolf-Rayet (WR) stars and are some of the most massive stars known, having $M_{\rm initial}$ >100 $M_\odot$, and prodigious winds, $\dot{M}$ >10^{-5} $M_\odot\,yr^{-1}$, that are enriched with helium and nitrogen; with these identifications, the Arches cluster contains about 5% of all known WR stars in the Galaxy. We find an upper limit to the velocity dispersion of 22 km s^{-1}, implying an upper limit to the cluster mass of 7(10^4) $M_\odot$ within a radius of 0.23 pc; we also estimate the bulk heliocentric velocity of the cluster to be $v_{\rm cluster,\odot}$ $\approx$ +95 km s^{-1}. Taken together, these results suggest that the Arches cluster was formed in a short, but massive, burst of star formation about 2.5±0.5 *Myr* ago, from a molecular cloud which is no longer present. The cluster happens to be approaching and ionizing the surface of a background molecular cloud, thus producing the Thermal Arched Filaments. We estimate that the cluster produces 4(10^{51}) ionizing photons s^{-1}, more than enough to account for the observed thermal radio flux from the nearby cloud, 3(10^{49}) ionizing photons s^{-1}. Commensurately, it produces $10^{7.8}$ $L_\odot$ in total luminosity, providing the heating source for the nearby molecular cloud, $L_{\rm cloud}$ $\approx$ 10^7 $L_\odot$. These interactions between a cluster of hot stars and a wayward molecular cloud are similar to those seen in the "Quintuplet/Sickle" region. The small spread of formation times for the known young clusters in the Galactic Center, and the relative lack of intermediate-age stars ($\tau_{\rm age}$=$10^{7.0}$ to $10^{7.3}$ yrs), suggest that the Galactic Center has recently been host to a burst of star formation. Finally, we have made new identifications of near-infrared sources that are counterparts to recently identified x-ray and radio sources.

Subject headings: Galaxy: center — techniques: spectroscopic — infrared: stars

---

[1]Based on observations with the NASA/ESA Hubble Space Telescope, obtained at the Space Telescope Science Institute, which is operated by the Association of Universities for Research in Astronomy, Inc. under NASA contract No. NAS5-26555.

[2]Data presented herein were obtained at the W.M. Keck Observatory, which is operated as a scientific

1. Introduction

The Arches cluster is an extraordinarily massive and dense young cluster of stars near the Galactic Center. First discovered about 10 years ago as a compact collection of a dozen or so emission-line stars (Cotera et al. 1992; Nagata et al. 1995; Figer 1995; Cotera 1995; Cotera et al. 1996), the cluster contains thousands of stars, including at least 160 O stars (Serabyn et al. 1998; Figer et al. 1999a). Figer et al. (1999a) used HST/NICMOS observations to estimate a total cluster mass ($\gtrsim 10^4\ M_\odot$) and radius (0.2 pc) to arrive at an average mass density of $3(10^5)\ M_\odot\ \mathrm{pc}^{-3}$ in stars, suggesting that the Arches cluster is the densest, and one of the most massive, young clusters in the Galaxy. They further used these data to estimate an initial mass function (IMF) which is very flat ($\Gamma \sim -0.6 \pm 0.1$) with respect to what has been found for the solar neighborhood (Salpeter 1955, $\Gamma \sim -1.35$) and other Galactic clusters (Scalo 1998). They also estimated an age of 2 ± 1 *Myr*, based on the magnitudes, colors, and mix of spectral types, which makes the cluster ideal for testing massive stellar-evolution models.

Given its extraordinary nature, the Arches cluster has been a target for many new observations. Stolte et al. (2002) recently verified a flat IMF slope for the Arches cluster, finding $\Gamma = -0.8$, using both adaptive optics imaging with the Gemini North telescope and the HST/NICMOS data presented in Figer et al. (1999a). Blum et al. (2001) used adaptive optics imaging at the CFHT and HST/NICMOS data (also presented in this paper) to identify several new emission-line stars and estimate an age for the cluster of 2−4.5 *Myr*. Lang, Goss, & Rodríguez (2001a) detected eight radio sources, seven of which have thermal spectral indices and stellar counterparts, within $10''$ of the center of the cluster. They suggest that the stellar winds from the counterparts produce the radio emission via free-free emission, consistent with earlier indications from near-infrared narrow-band imaging (Nagata et al. 1995) and spectroscopy (Cotera et al. 1996). In a related study, Lang, Goss, & Morris (2001b) argued that the hot stars in the Arches cluster are responsible for ionizing the surface of a nearby molecular cloud to produce the arches filaments, as originally suggested by Cotera et al. (1996) and Serabyn et al. (1998), but in contrast to earlier suggestions (Morris & Yusef-Zadeh 1989; Davidson et al. 1994; Colgan et al. 1996). Yusef-Zadeh et al. (2001) used the Chandra telescope to detect three x-ray components that they associate with the cluster, claiming that hot (10^7 K) x-ray emitting gas is produced by an interaction between material expelled by the massive stellar winds and the local interstellar medium.

---

partnership among the California Institute of Technology, the University of California and the National Aeronautics and Space Administration. The Observatory was made possible by the generous financial support of the W.M. Keck Foundation.

The Arches cluster has also been the target of several theoretical studies regarding dynamical evolution of compact young clusters. Kim, Morris, & Lee (1999) used Fokker-Planck models and Kim et al. (2000) used N-body models to simulate the Arches cluster, assuming the presence of the gravitational field of the Galactic Center. They found that such a cluster will disperse through two-body interactions over a 10 *Myr* timescale. Portegies-Zwart et al. (2001) performed a similar study and found a similar result, although they note the possibility that the Arches cluster is located in front of the plane containing the Galactic Center. Finally, Gerhard (2001) considered the possibility that compact clusters formed outside the central parsec will plunge into the Galactic center as a result of dynamical friction, eventually becoming similar in appearance to the young cluster currently residing there; Kim & Morris (2002) further consider this possibility.

In this paper, we use new and existing observations to determine the stellar properties of the most massive stars in the Arches cluster. We present astrometry and photometry of stars with estimated initial masses greater than 20 $M_{\odot}$ (the theoretical minimum mass of O stars), based upon HST/NICMOS narrow-band and broad-band imaging. We also present K-band high-resolution spectra of the emission-line stars, based upon Keck/NIRSPEC observations. We couple these data with previously-reported radio and x-ray data to infer stellar wind/atmosphere properties using a modeling code. Finally, we compare our results to those reported in recent observational and theoretical papers.

2. Observations

A log of our observations obtained using HST and KECK is given in Table 1.

2.1. HST

The HST data were obtained as part of GO-7364 (PI Figer), a program designed to measure the IMF's in the Arches and Quintuplet clusters (Figer et al. 1999a), determine the star-formation history of the Galactic Center (Serabyn et al. 2002), and determine the nature of the "Pistol Star" (Figer et al. 1999b).

Broad-band images were obtained using *HST*/NICMOS on UT 1997 September 13/14, in a 2×2 mosaic pattern in the NIC2 aperture (19.″2 on a side). Four nearby fields, separated from the center of the mosaic by 59″ in a symmetric cross-pattern, were imaged in order to sample the background population. All fields were imaged in F110W ($\lambda_{\rm center}$ = 1.10 μm), F160W ($\lambda_{\rm center}$ = 1.60 μm), and F205W ($\lambda_{\rm center}$ = 2.05 μm). The STEP256 sequence was

used in the MULTIACCUM read mode with 11 reads, giving an exposure time of ≈256 seconds per image. The plate scale was $0\farcs076$ pixel^{-1} (x) by $0\farcs075$ pixel^{-1} (y), in detector coordinates. The mosaic was centered on RA $17^{\rm h}45^{\rm m}50\fs35$, DEC $-28^\circ 49' 21\farcs82$ (J2000), and the pattern orientation was $-134\fdg6$. The spectacular F205W image is shown in Figure 1a, after first being processed with the standard STScI pipeline procedures.

The narrow-band images were obtained at roughly the same time as the broad-band images. One image was obtained in each of the F187N ($\lambda_{\rm center}$ = 1.87 μm) and F190N ($\lambda_{\rm center}$ = 1.90 μm) filters in the NIC2 aperture. The filters widths are 0.0194 μm for F187N and 0.0177 μm for F190N. We used the same exposure parameters for these images as those used for the broad-band images. The difference image, F187N minus F190N, is shown in Figure 2.

2.2. Keck

The spectroscopic observations were obtained on July 4, 1999, using NIRSPEC, the facility near-infrared spectrometer, on the Keck II telescope (McLean et al. 1998, 2002), in high resolution mode, covering *K*-band wavelengths (1.98 μm to 2.28 μm). The long slit ($24''$) was positioned in a north-south orientation on the sky, and a slit scan covering a $24''\times14''$ rectangular region was made by offsetting the telescope by a fraction of a slit width to the west between successive exposures. The slit-viewing camera (SCAM) was used to obtain images simultaneously with the spectroscopic exposures, making it easy to determine the slit orientation on the sky when the spectra were obtained. From SCAM images, we estimate seeing (FWHM) of $0\farcs6$. The plate scales for both spectrometer and SCAM were taken from Figer et al. (2000a). We chose to use the 3-pixel-wide slit ($0\farcs43$) in order to match the FWHM of the seeing disk. The corresponding resolving power was R∼23,300 ($=\lambda/\Delta\lambda_{\rm FWHM}$), as measured from unresolved arc lamp lines.

The NIRSPEC cross-disperser and the NIRSPEC-6 filter were used to image six echelle orders onto the 1024^2-pixel InSb detector. The approximate spectral range covered in these orders is listed in Table 2. Coverage includes He I (2.058 μm), He I (2.112/113 μm), Brγ/He I (2.166 μm), He II (2.189 μm), N III (2.24/25 μm), and the CO bandhead, starting at 2.294 μm and extending to longer wavelengths beyond the range of the observations.

Quintuplet Star #3 (hereafter "Q3"), which is featureless in this spectral region (Figer et al. 1998, Figure 1), was observed as a telluric standard (Moneti et al. 1994). Arc lamps containing Ar, Ne, Kr, and Xe, were observed to set the wavelength scale. In addition, a continuum lamp was observed through a vacuum gap etalon filter in order to produce an

accurate wavelength scale between arc lamp lines and sky lines (predominantly from OH). A field relatively devoid of stars (RA $17^{\rm h}\ 44^{\rm m}\ 49\overset{\rm s}{.}8$, DEC $-28^{\circ}\ 54^{\prime}\ 6\overset{\prime\prime}{.}8$, J2000) was observed to provide a dark current plus bias plus background image; this image was subtracted from each target image. A quartz-tungsten-halogen (QTH) lamp was observed to provide a "flat" image which was divided into the background-subtracted target images.

3. Data Reduction

3.1. Photometry

The NICMOS data were reduced as described in Figer et al. (1999a) using STScI pipeline routines, calnica and calnicb, and the most up-to-date reference files. Star-finding, PSF-building, and PSF-fitting procedures were performed using the DAOPHOT package (Stetson et al. 1987) within the Image Reduction and Analysis Facility (IRAF)[10]. For the narrow-band photometry, PSF standard stars were identified in the field and used in ALLSTAR. We used these stars to construct a model PSF with a radius of 15 pixels ($1.125''$). This model was then fitted stars found throughout the image using DAOFIND. Aperture corrections were estimated by comparing the magnitudes of the PSF stars with those from an aperture of radius 7.5 pixels ($0.563''$), and then adding $-2.5\log(1.159)$ in order to extrapolate to an infinite aperture (M. Rieke, priv. comm.). Table 1 gives the net aperture corrections to correct the aperture from a 3 pixel radius to infinity.

3.2. Source Identification and Astrometry

We culled the list produced by the process above by excluding stars with $A_{\rm K}<2.8$ or $A_{\rm K}>4.2$, or equivalently, stars with $m_{\rm F160W}-m_{\rm F205W}<1.4$ or $m_{\rm F160W}-m_{\rm F205W}>2.1$. These choices are motivated by the fact that the majority of stars in the Arches cluster have values within these limits, as can be seen in Figure 4 of Figer et al. (1999a); stars with values outside of these limits are likely to be foreground or background stars. The resultant star list is shown in Table 3. Objects are sorted according to inferred absolute K-band magnitudes, in order of decreasing brightness. K-band absolute magnitudes were calculated using $A_{\rm K} = {\rm E_{H-K}}/(A_{\rm H}/A_{\rm K}-1)$, where ${\rm E_{H-K}} = (H-K)-(H-K)_0$, and ${\rm A}_\lambda \propto \lambda^{-1.53}$ (Rieke

[10]IRAF is distributed by the National Optical Astronomy Observatories, which are operated by the Association of Universities for Research in Astronomy, Inc., under cooperative agreement with the National Science Foundation.

et al. 1989). We estimated intrinsic colors by convolving filter profiles with our best-matched model spectra. In cases where spectra were not available, i.e. for faint stars, $A_{\rm K} = 3.1$, a value that is supported by Figer et al. (1999a). This absolute magnitude was then translated into an initial mass according to the procedure in Figer et al. (1999a), except that we assumed solar metallicity, a decision supported by our quantitative spectroscopic analysis described later. Alternate identifications were taken from the following: Nagata et al. (1995), Cotera et al. (1996), Lang, Goss, & Rodríguez (2001a), and Blum et al. (2001). We had to allow as much as a $1''$ offset in some cases so that the correct objects coincided in the various data sets. The position offsets in the table are in right ascension (RA) and declination (Dec) and with respect to the star with the brightest inferred absolute magnitude at K. These offsets were calculated by applying the anamorphic plate scale at the time of observation and rotating x- and y- pixel offsets in the focal plane in to RA and Dec offsets in the sky. The stars are plotted and numbered in Figure 1b. Note that the masses in this table apply only in the case that the stars satisfy our model assumptions. This is not the case for some of the stars, especially the faint ones, given that they are likely to be field stars in the Galactic Center, but otherwise unassociated with the Arches cluster.

3.3. Narrow-band Imaging

The narrow-band filters cover wavelength regions that include several potentially relevant atomic transitions. There are potential contributions to the total observed flux through the F187N and F190N filters from 8 and 2 transitions (H I Paschen$-\alpha$, He I, and He II), respectively. It is clear from the broad feature near 2.166 μm that He I lines are strong in the spectra of the emission-line stars, while the relatively weak 2.189 μm line indicates that the He II lines falling in the F187N filter are minor contributors to $F_{\rm F187N}$. We estimate that the flux in the two lines falling in the F190N filter is negligible.

3.4. Narrow-band equivalent-widths

The equivalent-widths in Table 3 were computed according to the following equation:

$$EW_{1.87\ \mu{\rm m}} \ = \ \frac{(F_{\rm F187N} - F_{\rm F190N})}{F_{\rm F190N}} \times \Delta\lambda, \qquad (1)$$

where the fluxes are in W cm^{-2} μm^{-1} and $\Delta\lambda$ is the FWHM of the F187N filter; this equation assumes that the emission line(s) lie completely within the filter bandwidth, and that there is no contamination of $F_{\rm F190N}$ by emission or absorption lines. We increased $F_{\rm F187N}$ to account

for the difference in reddening for the two wavelengths, assuming the extinction law of Rieke et al. (1989); this correction is approximately 8.0% and depends slightly on the estimated extinction. In addition, we reduced $F_{\rm F187N}$ by 9.4% to account for the fact that the F187N filter has a shorter wavelength than the F190N filter and thus $F_{\rm F187N}$ will be greater by this amount than $F_{\rm F190N}$ for normal stars due to increasing flux toward shorter wavelengths on the Rayleigh-Jeans tail of the flux distributions at these wavelengths. Apparently, these two effects nearly cancel each other.

The difference image (F187N−F190N) in Figure 2 contains about two dozen emission-line stars with significant flux excesses in the F187N filter, as listed in Table 3. The narrow-band equivalent-widths increase with apparent brightness, as seen in Figure 3. In addition, the colors are redder as a function of increasing brightness (Figer et al. 1999a, Figure 4). Both effects are consistent with the notion that the winds are radiatively driven, so that higher luminosity stars will have stronger winds, and thus stronger emission lines, with commensurately stronger free-free emission which has a relatively flat (red) spectrum. In addition, the emission lines themselves contribute to a redder appearance. These effects are borne out in our models which show that a zero-age O star will have $m_{\rm F160W}-m_{\rm F205W}=-0.07$, while a late-type nitrogen-rich WR (WNL) star will have $m_{\rm F160W}-m_{\rm F205W}=+0.07$ from the continuum alone, and $m_{\rm F160W}-m_{\rm F205W}=+0.13$ from the emission-lines and continuum. So, a WNL star will have a color that is about +0.20 magnitudes redder than a zero-age O star. This agrees very well with the color trend seen in Figure 4, after one removes the stars with $m_{\rm F160W}-m_{\rm F205W}>1.85$; these stars are subject to extraordinary reddening, consistent with their location far from the cluster center and the behavior of reddening as a function of increasing distance from the center of the cluster (Stolte et al. 2002).

3.5. Spectroscopy

The spectra were reduced using IDL and IRAF routines. All target and calibration images were bias and background subtracted, flat fielded, and corrected for bad pixels. The target images were then transformed onto a rectified grid of data points spanning linear scales in the spatial and wavelength directions using the locations of stellar continuum sources and wavelength fiducials extracted from arc line images and continuum lamp plus etalon images. The rectified images were then used as inputs to the aperture extraction procedure. Finally, all 1D spectra were coadded and divided by the spectrum of a telluric standard to produce final spectra. The following gives a detailed description of this data reduction procedure.

A bias plus background image was produced from several images of a dark area of sky, observed with the same instrument and detector parameters as the targets. Because the sky

level was changing while these images were being obtained, we scaled the sky components before combining them with a median filter. The combined image was scaled in order to match the varying sky emission level in the target images and then added to the bias image formed by taking the median of several bias images. The resultant image was then subtracted from target images, thus subtracting properly scaled bias structure and background. This operation also removes dark current, although the subtraction will be perfect only in the case that the scaling factor for the varying sky level is exactly one. In other cases, a small residual in dark current will remain, although the amount of this residual will typically be less than 1 count (5 e^-).

Target images were divided by a normalized flat image, with bias structure and dark current first removed. We then removed deviant pixels from these images with a two-pass procedure. First, the median in a 5-by-5 pixel box surrounding each pixel was subtracted from every pixel in order to form an image with the low-spatial-frequency information removed. If the absolute value of a pixel in this difference image was larger than five times the deviation in the nearby pixels, then its value was replaced by the median data value in the box. The deviation in nearby pixels is defined as the median of the absolute values of those pixels in the difference image. On the second pass, isolated bad pixels were flagged and replaced if both the following were true: they were higher or lower than both immediate neighbors in the dispersion direction, and their value deviated by more than 10 times the square root of the average of those two neighbors. Isolated bad pixel values are replaced by the average values of their neighbors.

We rectified the target images by mapping a set of continuum traces and wavelength fiducials in the reduced images onto a set of grid points. This dewarping in both spatial and spectral directions is done simultaneously and requires knowledge of the wavelengths and positions of several spectral and spatial features; this information was extracted using arc, sky, or etalon lines. Typically, we identified 15 to 20 lines in each echelle order for this purpose. Two stellar continuum spectra and two flat-field edges traced across the length of the dispersion direction were used to define spatial warping. Rectification was done separately for each echelle order.

Unfortunately, there is a lack of naturally occurring, and regularly spaced, wavelength fiducials (absorption or emission lines) produced by the night sky or arc lamps. Because of this, we had to use a three-stage process for determining the relationship between column number and wavelength: rectify the images using the arc and sky lines, measure the etalon line wavelengths in the rectified version of the etalon image and obtain a solution to the etalon equation, and use the analytically determined wavelengths to produce a better rectification matrix. This approach gave results that were repeatable (to within an rms of $\sim$1 $\mathrm{km\,s^{-1}}$)

(Figer et al. 2002). This three-stage process is described in detail below.

In the first stage, we chose an order containing many (15 to 20) arc and sky lines so that wavelengths in the rectified images would be fairly well determined. The last few significant figures of some of the arc-line wavelengths, and all of the OH lines, out to seven significant figures, were derived from lists available from the National Institute of Standards and Technology (NIST) Atomic Spectra Database[11].

The process for fitting spectral lines was as follows. Each arc or sky line was divided into 10 to 20 sections along the length of the line. Rows from each section were averaged together, and the location of the peak was found by centroiding. Points along the line obtained from the centroiding were typically fitted with a 3rd-order polynomial. Outliers were clipped, and a new fit performed. We used a similar approach to fit the stellar and flat-field edge spatial traces.

We then used the arrays of coefficients from spatial and spectral fits to produce a mapping between points along the spectral features in the warped frame, and points in the dewarped frame. A two-dimensional second or third order polynomial was then fitted to these points, resulting in a list of transformation coefficients, the "rectification matrix."

In the second stage, after dewarping the etalon image with the rectification matrix produced from the arc and sky lines, we measured the wavelength of each etalon line using SPLOT in IRAF. This provided preliminary estimated wavelengths for each etalon line. Exact etalon wavelengths were given by the etalon equation. Solutions to the etalon equation were found using the constraint that features must have integer order numbers that decrease sequentially toward longer wavelengths. The estimated wavelengths of the 14 to 16 lines were used to produce a series of etalon equations that we simultaneously solved by finding the thickness and order numbers giving the least overall variance from the measured wavelengths. Once these parameters were determined, exact wavelengths could be calculated for each etalon line.

In stage three, the exact etalon wavelengths were used to determine a new rectification matrix by tracing these features in the rectified etalon image. Together with the same spatial information used to produce the first stage rectification matrix, a new rectification matrix was produced. The improved quality of the etalon lines allowed for a higher order (fourth or fifth order) polynomial fit to the etalon mapping between warped and dewarped points. The new matrices were applied to the appropriate spectral orders of target images.

Three images of the telluric standard ("Q3") were taken using the same setup as was

[11]http://physics.nist.gov/PhysRefData/ASD1/nist-atomic-spectra.html

used to obtain the target images. We moved the telescope along the slit length direction between exposures so that the spectra were imaged onto different rows of the detector. We reduced these images using the sames procedures used for reducing the target images.

Finally, APALL (IRAF) was used to extract spectra in manually chosen apertures. The resultant 1D spectra were then coadded in the case that a single object was observed in multiple slit positionings. Before coadding, we shifted all spectra to a common slit position by cross-correlating the telluric absorption features and shifting the spectra. The coadded spectra of all the stars in Table 3 for which we have spectra are shown in Figure 5; note that these spectra have been smoothed using an 11-pixel (44 $\mathrm{km\,s^{-1}}$) square boxcar function for display purposes. The fluxes were not reddening-corrected, so the spectral shape (roughly flat) is indicative of a hot star observed through a large amount of extinction.

4. Results

We use the data in this paper to form a census of stellar types for massive stars in the cluster, estimate physical properties of the stars, determine the dynamical state of the cluster members, and assess the impact of the cluster on its environment.

4.1. Spectral Types

The spectra for the most massive stars in our data set are relatively similar, although the features have smaller equivalent-widths for fainter stars. The brightest stars generally have spectra with a weak feature near 2.058 μm (He I), weak emission near 2.104 μm (N III) and 2.112/113 μm (He I), broad and strong emission near 2.166 μm (He I, H I), a weak line near 2.189 μm in P-Cygni profile (He II) in some cases, and weak lines at 2.115/2.24/2.25 μm (N III), where the primary contributors to the emission line fluxes are due to transitions of species listed in parentheses. There are indications of absorption at 2.058 μm in most of the first ten stars, and in some cases, it is strongly in a P-cygni profile (#3 and #8). In both these cases, the absorption appears to have a "double-bottom." This line and the 2.112/113 μm blend are narrow in the spectra of #10, #13, #15, and #29.

From these spectra alone, we might assign spectral types of WNL (WN7−WN9) (Figer, McLean, & Najarro 1997) or O If$^+$ (Hanson et al. 1996) for the brightest stars, just as have been assigned in Nagata et al. (1995) and Cotera et al. (1996); the degeneracy in the classification of stars of these spectral types was noted by Conti et al. (1995). Figure 6 compares an average spectrum of the Arches stars with those of WNL stars (Figer, McLean,

& Najarro 1997) and O If$^+$ stars (Hanson et al. 1996). We can see that the Arches stars have N III emission at 2.104 μm, 2.24 μm, and 2.25 μm, just like that seen in the spectra of WN7−8 stars, while the spectra of the O If$^+$ stars do not have those lines in emission (or they are very weak). Figer, McLean, & Najarro (1997) argued that N III lines in the K-band might be used to distinguish Wolf-Rayet (WR) from O If$^+$ stars on both observational and theoretical grounds. In addition, Figer, McLean, & Najarro (1997) showed that WN stars separate by subtype as a function of the relative line strengths in certain lines of their K-band spectra, i.e. $W_{2.189\,\mu m}/W_{2.166\,\mu m}$ or $W_{2.189\,\mu m}/W_{2.11\,\mu m}$. The relevant values for spectra of the most massive Arches stars are consistent with classifications of WNL. In addition, the equivalent-widths measured for the emission lines are in the range of those measured for WNL stars in Figer, McLean, & Najarro (1997), but not for O If$^+$ stars. From all these measures, we conclude that the Arches stars are WN9 types, with an uncertainty of ± one subtype. Later in this paper, we use wind/atmosphere models to show that the estimated nitrogen, carbon, and helium abundances verify WNL classifications.

One objection to the WNL classification might be that it is improbable that all the WR stars in the cluster be in the exact same evolutionary phase, i.e. WNL. Actually, such a situation is predicted by Meynet (1995). Indeed, our new observations show that there are no WR stars in the cluster other than the WNL types, given that our narrow-band observations would easily detect the strong emission lines from all WR stars, such as the WNE star in the Quintuplet cluster (Figer, McLean, & Morris 1995), or the carbon-rich WR (WC) stars seen near the Pistol Star (Figer et al. 1999b). The lack of WC stars suggests an age less than 3.5 *Myr* (Meynet 1995), consistent with the WNL classification for brightest stars in the Arches cluster.

We have identified two groups among the most massive stars with spectral types distinctly different than the WN9 spectral type. The group of stars from #10 to #30 are O If$^+$ types, and fainter stars are O main sequence stars.

4.2. Identification of the Main Sequence in the Galactic Center

The fainter stars in Table 3 (ID>30) appear to have little to no excess emission at 1.87 μm, consistent with the fact that their spectra appear to be relatively flat. Indeed, some even show absorption at 2.058 μm, 2.112 μm, and 2.166 μm, of a few angstroms equivalent width. In the case of star #68, the spectrum (Brγ absorption), apparent magnitude, and extinction, suggest a luminosity and temperature consistent with an initial mass of about 60 $M_\odot$, and its presence on the main sequence, given an age of 2.5 *Myr* and the Geneva models. The star is likely to be a late-O giant or supergiant, albeit still burning hydrogen

in its core, and thus its classification on the main sequence; note that it is too bright to be a dwarf. There are several other similar stars that have relatively featureless spectra, consistent with the spectra of O main sequence stars. This result is a significant spectroscopic verification of the claim in Figer et al. (1999a) that the main sequence is clearly visible in the broadband NICMOS data; also, note that Serabyn, Shupe, & Figer (1999) identified likely O stars with spectra that appeared to be featureless at the resolution of their observations. While a possible identification of the main sequence in the Galactic Center has previously been claimed (Eckart et al. 1999; Figer et al. 2000a), the result in this paper is the first spectroscopic identification of single stars that are unambiguously on the main sequence, as observed by their narrow absorption lines.

4.3. Wind/atmosphere Modelling

To model the massive Arches stars and estimate their physical parameters, we have used the iterative, non-LTE line blanketing method presented by Hillier & Miller (1998). The code solves the radiative transfer equation in the co-moving frame for the expanding atmospheres of early-type stars in spherical geometry, subject to the constraints of statistical and radiative equilibrium. Steady state is assumed, and the density structure is set by the mass-loss rate and the velocity field via the equation of continuity. We allow for the presence of clumping via a clumping law characterized by a volume filling factor f(r), so that the "smooth" mass-loss rate, $\dot{M}_S$, is related to the "clumped" mass-loss rate, $\dot{M}_C$, through $\dot{M}_S$=$\dot{M}_C$/f$^{1/2}$. The velocity law (Hillier 1989) is characterized by an isothermal effective scale height in the inner atmosphere, and becomes a β law in the wind. The model is then prescribed by the stellar radius, R_*, the stellar luminosity, L_*, the mass-loss rate $\dot{M}$, the velocity field, $v(r)$, the volume filling factor, f, and the abundances of the elements considered. Hillier & Miller (1998, 1999) present a detailed discussion of the code. For the present analysis we have assumed the atmosphere to be composed of H, He, C, N, Mg, Si and Fe.

We created a grid of models within the parameter domain of interest. It was bounded by 4.4<log($T_{\rm eff}$)<4.6, 5.0≤log($L_*/L_\odot$)≤6.5, −5.7≤log($\dot{M}/M_\odot\ yr^{-1}$)≤−3.8 , 0.25≤H/He≤10, and 1≤Z/$Z_\odot$≤2. This grid was used as a starting point to perform detailed analyses of the objects, for which the grid parameters were fine tuned, and other stellar properties such as the velocity field and clumping law were relaxed. The observational constraints were set by the NIRSPEC K-band spectra, and the NICMOS F187W equivalent-width and continuum (F110W, F160W and F205W) values.

We present preliminary results for stars #8 and #10. A complete, detailed analysis of the whole sample will be discussed in Najarro et al. (2002). Table 4 shows the stellar

parameters derived for stars #8 and #10, while Figures 7a,b show the excellent fits of the models to the observed spectra. All stellar parameters for the strong-line-emission object (#8) displayed in Table 4 should be regarded as rather firm with the exception of the carbon abundance which should be considered as an upper limit. For star #10, however, no information can be obtained about its terminal velocity and clumping factor. Further, only upper limits are found again for the carbon abundance, while the uncertainty in the nitrogen abundance is rather high, up to a factor of 3, due to the extreme sensitivity of the N III lines to the transition region between photosphere and wind in this parameter domain. Therefore we have assumed the star to have a terminal velocity of 1000 $\mathrm{km\,s^{-1}}$, which is representative of this class of objects, and a filling factor of f = 0.1 as derived for object #8. To illustrate how the assumption of different clumping factor or v_∞values can affect the derived stellar parameters, we also show in Table 4 two additional models which match as well the observed spectra with modified f (f=1, #10b) and terminal velocity (v_∞=1600 $\mathrm{km\,s^{-1}}$, #10c). Note that there is no simple $\dot{M}_{C1}/{\mathrm{f}_1}^{1/2} = \dot{M}_{C2}/{\mathrm{f}_2}^{1/2}$ scaling (Herald, Hillier, & Schulte-Ladbeck 2001) nor $\dot{M}_1/v_{\infty 1} = \dot{M}_2/v_{\infty 2}$ scaling between the models, and that other stellar parameters require readjustment.

Table 4 reveals that objects #8 and #10 have very similar luminosities, temperatures, and ionizing-photon rates. However, their wind densities ($\dot{M}$) and abundances reveal different evolutionary phases for these two objects. Object #8 fits well with a WNL evolutionary stage. Its wind density and helium abundance are very similar to those derived by Bohannan & Crowther (1999) for WN9h stars. On the other hand, object #10 can be placed into a O If$^+$ phase as its wind density is roughly an order of magnitude lower than that of object #8 and the derived He abundance and upper limits for nitrogen enrichment indicate an earlier evolutionary phase. Indeed, its K-band spectrum is nearly identical to that of the O8 If$^+$ star HD151804 (Hanson et al. 1996). Interestingly, both Arches objects have luminosities about one magnitude larger than their counterparts in Bohannan & Crowther (1999).

4.4. Ionizing Flux

Containing so many massive stars, the Arches cluster produces a large ionizing flux. We estimate the total ionizing flux emitted by the cluster to be $4(10^{51})$ photons $\mathrm{s^{-1}}$, based on our wind/atmosphere model fits for the two emission-line stars in Table 4. To estimate the total flux, we multiplied the estimated ionizing flux from #8 by 10, that from #10 by 20, and determined those of the remaining stars in Table 3 by applying equation 3 in Crowther & Dessart (1998); these factors reflect our choice of #8 and #10 as representatives of the first 30 stars in the table. The ionizing flux estimate is a bit higher than that in Serabyn et

al. (1998), ≈ a few 10^{51} photons s^{-1}, after scaling that number for the fact that the cluster contains 50% more O stars than originally thought (Figer et al. 1999a). This amount of ionizing flux is consistent with the Arches cluster being the ionizing source for the Thermal Arches Filaments (Lang, Goss, & Morris 2001b).

4.5. Luminosity

Using the same process as applied to estimate the cluster ionizing flux, we estimate a total cluster luminosity of $10^{7.8}$ $L_{\odot}$, or one of the most luminous clusters in the Galaxy. About 40% of the total luminosity is contributed by the 30 brightest stars in Table 3.

4.6. Age

As described in Figer et al. (1999b), the absolute magnitudes and mix of spectral types are consistent with a cluster age of 2 ± 1 *Myr*. This was estimated using the colors and magnitudes of the stars, i.e. the colors give the extinction value, and the apparent magnitudes lead to absolute K-band magnitudes, which are then compared to isochrones from the Geneva models (Meynet et al. 1994). It is possible for older stars to attain magnitudes as bright as the brightest stars in the cluster, but only at relatively cool temperatures, i.e. $T_{\rm eff} < 25$kK. A new age constraint from the data in this paper is given by the absence of WC or WNE stars in the cluster. This observational constraint, when combined with the models of Meynet (1995), gives $\tau_{\rm age} < 3.0$ *Myr* for the least limiting case ($2\times\dot{M}$, Z=0.040) and $\tau_{\rm age} < 2.5$ *Myr* for the most limiting case ($1\times\dot{M}$, Z=0.040). In addition, the presence of WNL stars requires $\tau_{\rm age} > 1.5$ *Myr* from these models. Finally, we note the lack of relatively cool (B-type) supergiant emission-line stars, such as those found in the central parsec (Krabbe et al. 1995) and the Quintuplet cluster (Figer et al. 1999b). The lack of such stars in the Arches cluster implies $\tau_{\rm age} < 4.0$ *Myr*. Finally, the detailed model for star #8 suggests an age of 2.5 *Myr*, at least for that star. We combine all this evidence to suggest that the cluster age is 2.5 ± 0.5 *Myr*, where the error is dominated by our lack of information concerning metallicity.

4.7. Velocities

A velocity determination for the emission-line stars is complicated by several facts. First, the strongest spectral features are blended emission lines, making it impractical to simply

compare the measured wavelength centroid of a "line" to the expected vacuum wavelength. Because of this, one must cross-correlate the target spectra with respect to a template spectrum composed of features that accurately represent relative strengths of the blended lines. Second, the emission lines are broad, so that small wavelength shifts will produce little change in the cross-correlated power when compared to a template spectrum. Third, there are slight differences in the shapes of the emission lines between spectra of the various stars, so a model blend for one spectrum might not faithfully reproduce the features in another spectrum, at least not to the fidelity required for high precision velocity measurements. Because of these difficulties, we approached the velocity estimates using two techniques. We smoothed the spectra using a box-car filter with varying widths between 1 and 31 pixels (4 and 120 $\mathrm{km\,s^{-1}}$), finding little difference in the velocities as a function of these widths.

First, we estimated an absolute velocity for star #8 by cross-correlating its spectrum with that of our model spectrum. This method gave a velocity of $+54$ $\mathrm{km\,s^{-1}}$ (redshifted), in the heliocentric frame, for the blend near 2.166 μm. Our estimates using other lines are somewhat less than this value, as low as $+20$ $\mathrm{km\,s^{-1}}$, but those lines are weaker than the blend at 2.166 μm, and thus produce larger velocity errors.

In the second method, we cross-correlated all the spectra against each other. The cross-correlations were performed separately on three wavelength regions, the first containing the 2.104 μm and 2.115 μm features, the second containing the 2.166 μm and 2.189 μm features, and the third containing the doublet at 2.25 μm. This method was used to compute the standard deviation of relative velocities, allowing us to infer the mass enclosed within some orbital radius that represents an average of the emission-line stars' orbital radii. Given that small differences in intrinsic blend morphology can affect the location of the maximum point of the cross-correlated power, we also repeated this approach using line centroids to compute velocity differences. Using both approaches, we found a standard deviation of $\approx$22 $\mathrm{km\,s^{-1}}$ for a sample containing eight emission-line stars. This value represents an upper limit on the intrinsic dispersion, given that the effects described above would tend to increase the estimated value over the intrinsic velocity dispersion. We also found that the stars were redshifted by $+41$ $\mathrm{km\,s^{-1}}$ with respect to star #8. We therefore estimate a heliocentric "cluster" velocity of $+95\pm8$ $\mathrm{km\,s^{-1}}$, where the error is simply the standard deviation divided by the square root of eight; note that this error neglects the systematic effects described above, so the true velocity might differ from the estimate by significantly larger than the quoted error.

For a gravitationally bound and spherically symmetric cluster of mass $\mathrm{M_{cluster}}$, the virial theorem gives $\mathrm{M_{cluster}} = 3\sigma^2\mathrm{R/G}$ (Ho and Filippenko 1996), where σ is the one-dimensional velocity dispersion, R is the appropriate radius, G is the gravitational constant, the ve-

locities are assumed to be isotropic, and all stars have equal mass. This simple formula can be compared to the more general case where the cluster can be resolved into individual stars (Illingworth 1976). Using R = 0.23 pc for the sample in question, we calculate $M_{cluster} < 7(10^4)\ M_{\odot}$, or about five times greater than what would be expected from direct integration of the mass function in Figer et al. (1999a) over the area sampled by the stars used in the analysis. This high mass limit results from the systematic effects inherent in our radial velocity determinations, as described above.

5. Discussion

In this section, we compare our measurements to those in previous papers and use measurements at other wavelengths to determine the physical parameters of the observed stars. Finally, we discuss how the Arches cluster interacts with its local environment to create heating and ionization of a nearby cloud.

5.1. Comparison to Previous Near-infrared Measurements

Table 3 lists over 30 probable emission-line stars, albeit the faintest having relatively weak emission lines; Figure 3a confirms that there are roughly this number of stars with reliable emission-line excesses. This list contains over a factor of two increase in the number of emission-line stars previously identified in the cluster (Blum et al. 2001; Nagata et al. 1995; Cotera et al. 1996). The line and continuum fluxes presented here largely agree with earlier results (Nagata et al. 1995; Cotera et al. 1996). The $F_{\rm F187N}$ and $F_{\rm F190N}$ fluxes reported in this paper are similar to those reported in Blum et al. (2001), after correcting for differences in the assumed zero points, the fact that we corrected for the difference in extinction at the two narrow-band wavelengths, and that we also corrected for the intrinsic shape of the stellar continuum; in addition, our extinction estimates are higher in many cases than those used in Blum et al. (2001).

The spectra in this paper are consistent with the narrow-band photometry in Nagata et al. (1995) and Blum et al. (2001) and the spectra in Cotera et al. (1996), although our high-resolution spectroscopy shows that the photometry is significantly affected by blending of absorption and emission features in P-Cygni profiles.

We confirm the discovery of a new bright emission-line star (#5, B22, N9) near the southern edge of the cluster, reported in Blum et al. (2001), and note that it is a counterpart of the x-ray source, "AR8," in Lang, Goss, & Rodríguez (2001a). We also confirm that star

#16 (B19) is an emission-line star, as suspected by Blum et al. (2001). Blum et al. (2001) listed some additional candidate emission-line stars. We confirm that the following stars from that list are, indeed, emission-line stars (their designations in parentheses): #15 (B8), #27 (B16), #17 (B29), #10 (B30), #10 (B20), #13 (B31).

5.2. Comparison to X-ray Flux Measurements

Yusef-Zadeh et al. (2001) reported Chandra X-ray observations of a region including the Arches cluster. They detected three extended sources, one (A1) near the center of the Arches cluster, another (A2) located to the North and West of the center by about 7″ and a third weaker source (A3) about 90″ × 60″ in size underlying the first two. The centroid of source A2 coincides within 1 arcsecond with an emission-line star, #9 in Table 3. The apparent spatial coincidence of the X-ray sources and Arches cluster strongly suggests that the X-ray sources are physically associated with the cluster. Yusef-Zadeh et al. estimate the total X-ray luminosity between 0.2 and 10 keV to be 3.3, 0.8 and 0.16 (10^{35}) ergs s^{-1} for A1, A2 and A3, respectively. They attribute the emission from A1 and A2 to either colliding winds in binary systems or to the winds from single stars interacting with the collective wind from the entire cluster. The coincidence of source A2 with an emission-line source is very interesting in the context of the latter scenario. A3, on the other hand, has roughly the characteristics expected from shock-heated gas created by the collisions of the multitude of 1000-km s^{-1} stellar winds emanating from the stars in the rich, dense cluster (Ozernoy, Genzel, & Usov 1997; Cantó, Raga, & Rodríguez 2000). Because the X-ray sources are extended, it is unlikely that they can be attributed to single X-ray binary systems. However, the rough coincidence of source A1 with the core of the cluster raises the possibility that it may be comprised of many relatively weak stellar X-ray sources, binary or single, residing in the cluster core, and unresolved spatially from each other.

5.3. Comparison to Radio Flux Measurements

From Table 3 we see that one of the objects analysed in this work, #8, has also been detected at 8.5 GHz (Lang, Goss, & Rodríguez 2001a). Our derived mass-loss rate is consistent with the observed radio flux (0.23 mJy) only if the outer wind regions are unclumped. Such a behavior for the clumping law has been suggested by Nugis, Crowther, & Willis (1998) from analysis of galactic WR stars. They found that the observed infrared to radio fluxes of WR stars are well reproduced by a clumping law where the filling factor is unity close to the stellar surface, increasing to a minimum at 5 to 10 R_* and returning again to unity

in the outer wind where the radio flux forms. Note, however, that the line fluxes of the weaker lines like Brγ or He I remain unaltered with this new description of the clumping law, but the line fluxes of the strongest lines, such as Paα, formed in the outer wind can be significantly reduced. From Table 4 we see that our models are fully consistent with the observed equivalent-width of Paα.

We consider now the possible correlation between line fluxes and radio-continuum flux analogous to the one discussed above for K-band fluxes (see Figure 3a). In principle, we also expect the near-infrared emission line strengths to scale with the free-free emission detected at radio wavelengths (Nugis, Crowther, & Willis 1998; Leitherer, Chapman, & Koribalski 1997). However, we do not find such a correlation, as can be seen in Figures 8a,b. A similar result was obtained by Bieging, Abbott, & Churchwell (1982) for a sample of eight WR stars. We believe this apparent absence of correlation between Paα line-strength and radio flux is caused by both observational and physical effects. The observational effect is related to the fact that the radio measurements are picking up only the tip of the iceberg, i.e., those stars with the densest winds of the cluster. The physical effect is related to the fact that all three components contributing to $\mathrm{EW}_{1.87\mu\mathrm{m}}$ (H I, He I, and He II) are very sensitive to changes in temperature in the parameter domain appropriate to these objects. Further, both the line and continuum fluxes depend strongly not only on the mass-loss rate but also on the shape of the velocity field and the clumping law. Therefore, such strong dependence of the Paα line flux on several stellar parameters introduces a large scatter in the expected line-strength vs radio-flux relationship.

The radio fluxes of the most massive Arches stars are comparable to those of WNL stars, but not to those of O If$^+$ stars. The WN8 star WR105 (van der Hucht 2001) would emit 0.14 mJy at the distance of the Arches cluster, comfortably within the range of fluxes measured for the Arches stars. Similar values are reported for WR stars in Bieging, Abbott, & Churchwell (1982). On the other hand, HD 16691 (O4 If$^+$) emits 0.3 mJy at 4.9 GHz, according to Wendker (1995), implying an expected flux of 1.7 μJy at the distance of the Arches cluster, assuming that the star has a parallax of 1.7 mas (Perryman et al. 1997). The expected flux is two orders of magnitude below the flux levels of the brightest Arches stars (Lang, Goss, & Rodríguez 2001a). No doubt, this difference is due to the relatively low mass-loss rate for HD 16691, about 1/20 of that of the bright Arches stars. A similar trend can be seen in Figure 6 where the emission lines in the spectra of HD 16691 are shown to be much weaker than those in the spectra of the Arches emission-line stars. Again, weak winds produce weak emission lines and weak free-free emission.

Finally, we report several additional radio sources having emission-line star counterparts. They were found by comparing the radio continuum contour plot in Lang, Goss, & Rodríguez

(2001a) with the difference image in Figure 2; they are marked by squares in this figure. We have designated the four near-infrared counterparts to these newly identified radio sources in Table 3.

5.4. Evolutionary Status of the Massive Stars in the Arches Cluster

The emission-line stars appear to contain significant amounts of hydrogen, while also exhibiting considerable helium content. We believe that this can be explained by the most massive stellar models in Meynet et al. (1994). For the brightest 10 or so stars in Table 3, the observations can be fit by these models for $M_{\rm initial}{\gtrsim}120\ M_\odot$ stars that have evolved to cool temperatures while retaining hydrogen. In particular, star #8 can be fit by a $M_{\rm initial}{\sim}120\ M_\odot$ star with solar abundance, standard mass-loss rates, age of 2.4 *Myr* to 2.5 *Myr*, and present-day mass of 72 $M_\odot$ to 76 $M_\odot$ (Schaller, Schaerer, Meynet, & Maeder 1992).

5.5. Relation to the Nearby Molecular Cloud (M0.10+0.03)

It appears that the Arches cluster heats and ionizes the surface of M0.10+0.03, the nearby molecular cloud (Serabyn & Guesten 1987; Brown & Liszt 1984), given that the cluster can easily provide the necessary flux to account for the infrared emission and recombination-line flux from the cloud.

The relative heliocentric velocity between the cluster stars ($+95{\pm}8$ km s^{-1}) and the ionized gas on the surface of the cloud (-20 to -50 km s^{-1}) suggests that the physical association is accidental and that the cluster stars are ionizing the surface of the cloud. This difference in velocity is reminiscient of that observed between the Quintuplet ($+130$ km s^{-1}) (Figer 1995; Figer et al. 1999a) and the Sickle cloud, M0.10+0.03 ($+30$ km s^{-1}) (Lang, Goss, & Wood 1997). In both cases, it appears that young clusters happen to lie near molecular clouds whose surfaces are ionized by the photons from the hot stars in the clusters. The following shows that the ionizing flux and energy required to heat the cloud can be provided by the Arches cluster. Note that a differential velocity of 100 km s^{-1} would produce a relative drift of 100 pc in 1 *Myr*, a distance that would bring a cluster within the vicinity of a few clouds, given the spatial distribution of clouds in the central few hundred parsecs.

5.5.1. Ionization and Heating

Even before the discovery of the Arches cluster, Serabyn & Guesten (1987), Genzel et al. (1990), and Mizutani et al. (1994) suggested that the Thermal Arched Filaments are photoionized by nearby hot stars. After the discovery of the cluster, many authors considered the possibility that the cluster is ionizing the cloud. One problem with this idea is the fact that the filaments are very large, and have roughly constant surface brightness and excitation conditions (Erickson et al. 1991; Colgan et al. 1996), indicating that the ionizing source is either evenly distributed over many parsecs or is relatively far away. Given the new ionizing flux estimates in this paper and in (Serabyn et al. 1998), the cluster would produce enough flux to account for the filaments, even if 20 pc away, far enough to allow for the even illumination that is observed. Indeed, Timmermann et al. (1996) predicted this result, and Lang, Goss, & Morris (2001b) present a detailed analysis that confirms it.

Cotera et al. (1996) give estimates for the total ionizing flux of $2{-}5(10^{50})$ photons s^{-1}, depending on whether one models the spectral energy distributions for the emission-line stars with Kurucz (1979) atmospheres or blackbody functions; however, this estimate includes only flux from the dozen or so emission-line stars that were known at the time. Nonetheless, the results of this paper suggest that the cluster ionizes the cloud.

The heating in the cloud produces an infrared luminosity of 10^7 $L_\odot$ (Morris, Davidson, & Werner 1995). Assuming a covering fraction of $\approx$10%, we find that the Arches cluster can deliver about this much luminosity, within a factor of two.

5.5.2. Location along the line of sight

Given the Brγ flux from the filaments measured by Figer (1995), we know that the line emission is extincted by about $A_{\rm K}{\sim}3$. This implies that the filaments are on the near side of the cloud, since such an extinction corresponds only to the typical foreground extinction to the Galactic Center, and precludes any substantial additonal extinction. This information leads to the conclusion that the Arches cluster is on the near side of, and is approaching, the wayward molecular cloud that is moving in opposition to the bulk motion of stars and gas around the Galactic Center (McGinn, Sellgren, Becklin, & Hall 1989), consistent with the geometry described in Lang, Goss, & Morris (2001b).

5.6. Dynamical Evolution and Uniqueness of the Arches and Quintuplet Clusters

The temporal coincidence of the star formation events that produced the massive clusters in the Galactic Center, and the lack of older red supergiants, suggest that the Galactic Center has been host to a recent burst of star formation. Kim, Morris, & Lee (1999) and Kim et al. (2000) predicted that compact young clusters in the Galactic Center would evaporate on short timescales, i.e. a few *Myr*. Portegies-Zwart et al. (2001) argue that other clusters similar to, yet somewhat older than, the Arches and Quintuplet clusters exist in the central 100 pc. This argument is based upon a dynamical analysis which predicts that such clusters evaporate after 55 *Myr*, and further that the clusters' projected surface number density in stars drops below the limit of detectability in a few *Myr*. The statement that members of dispersed clusters could have gone undetected is incorrect. Such stars would easily be detectable for their extreme brightness, i.e. there would be hundreds of stars as bright as IRS 7 (in the central parsec) strewn about the central 100 pc for each Arches/Quintuplet-like cluster between the age of 5 and 30 *Myr*. Given the claim in Portegies-Zwart et al. about the expected number of "hidden" young clusters in the central hundred parsecs, we would expect to see of order ten thousand red supergiants in this region. Only a few are seen, as demonstrated by surveys for such stars (Figer 1995; Cotera 1995).

Portegies-Zwart et al. suggest that clusters could be "hiding" near bright stars due to limitations in dynamic range, but these arguments are specious, since the dynamic range of array-based detections are obviously not limited by the digitization of a single read if multiple coadds are used (e.g. Figer et al. (1999a) reach a dynamic range of over 10^5). Thus in agreement with Kim et al., we conclude that the clusters must disperse rapidly

5.7. Comparison to NGC 3603 and R136 in 30 Dor

The Arches cluster is similar in age and content to NGC 3603 and R136 in 30 Dor, and is surrounded by a giant H II region as is R136. In contrast to these clusters, we do not see WN5h or WN6h stars (Crowther & Dessart 1998), suggesting that the Arches cluster is older. This is consistent with our age determination, as suggested by other means described earlier.

While our spectra exhibit no primary diagnostic lines to estimate metallicity, we may use our estimates for the helium and nitrogen abundances in object #8 in conjunction with the evolutionary model for 120 $M_\odot$ to infer metallicity. For Z(He)=0.7, the models predict the star to have already reached its maximum nitrogen surface mass fraction. Hence, we

may compare our derived nitrogen mass fraction, Z(N)=0.016, with the evolutionary models values at different metallicities (Schaller, Schaerer, Meynet, & Maeder 1992). We see that this value is met for solar metallicity. A more detailed analysis of the metallicity of the Arches stars will be presented in Najarro et al. (2002).

We thank Nolan Walborn and Nino Panagia for critical readings of the paper. We thank John Hillier for providing his code. F. N. acknowledges DGYCIT grants ESP98-1351 and PANAYA2000-1784. We acknowledge the work of: Maryanne Angliongto, Oddvar Bendiksen, George Brims, Leah Buchholz, John Canfield, Kim Chin, Jonah Hare, Fred Lacayanga, Samuel B. Larson, Tim Liu, Nick Magnone, Gunnar Skulason, Michael Spencer, Jason Weiss and Woon Wong.

Table 1. Log of Observations

Type	Filter[a]	$\lambda_{\rm center}$ μm	PHOTFNU/ZP(Vega)[b] sec. DN^{-1}	Ap. Corr. 3 pix. to inf	Integ.	Date
Spectroscopy[c]	NIRSPEC-6	K-band	···	···	150 s.	3 July 1
Imaging	F110W	1.10	9.61E-10	1.35	256 s.	13 September 1
Imaging	F160W	1.60	1.86E-09	1.67	256 s.	13 September 1
Imaging	F205W	2.05	1.64E-09	1.81	256 s.	13 September 1
Imaging	F187N	1.874	4.95E-08	1.75	256 s.	13 September 1
Imaging	F190N	1.900	5.36E-08	1.76	256 s.	13 September 1

[a]NIRSPEC-6 has half-power points of 1.85 μm and 2.62 μm (Figer et al. 2000b). Because the order longer than the width of the detector, the spectra are not contiguous in wavelength.

[b]Multiplying PHOTFNU/ZP(Vega) by the observed count rate gives the ratio of the object's flux with re to Vega. Values for F110W, F160W, and F205W are from the HST Data Handbook (Keyes et al. 1997). V for F187N and F190N are from Marcia Rieke (priv. communication). The zero points in Blum et al. (2 were also provided by Marcia Rieke; however, the values used in the table above were more recently provi

[c]All spectroscopy images were obtained with the slit positioned approximately north-south using the mu correlated read mode ("Fowler" sampling) with 16 reads at the beginning and end of each integration. resolution was 23,300, ($\lambda/\Delta\lambda_{\rm FWHM}$, where $\Delta\lambda_{\rm FWHM}$ is the full-width at half maximum of unresolved arc lines). The slit size was $0\farcs43 \times 24''$.

Table 2. Wavelength Coverage in Spectra

Echelle Order	$\lambda_{\rm min}$ μm	$\lambda_{\rm max}$ μm
33	2.281	2.315
34	2.214	2.248
35	2.152	2.184
36	2.092	2.124
37	2.036	2.067
38	1.983	2.013

Table 3. Massive Stars in Arches Cluster

ID[a]	Desig./Ref.[b]	ΔRA[c]	ΔDEC[c]	m_{F110W}	m_{F160W}	m_{F205W}	M_K[d]	M_{init}[e]	EW[f]	$ergs$
		″	″	mag.	mag.	mag.	mag.	$M_\odot$	$\mathring{A}$	
(1)	(2)	(3)	(4)	(5)	(6)	(7)	(8)	(9)	(10)	
1	N4 C9 AR3 B28	0.″00	0.″00	16.30	12.33	10.45	−8.0	>120	128.2	
2	N1 C13 AR17 B34	−6.″75	−3.″53	17.84	13.39	11.18	−7.9	>120	152.3	
3	N14 C11 AR7 B3	8.″20	−4.″13	16.06	12.28	10.46	−7.7	>120	218.2	
4	N11 C2 AR5 B17	4.″83	4.″66	15.63	12.12	10.37	−7.6	>120	230.5	
5	N9 AR8 B22	3.″29	−9.″64	16.69	12.80	10.86	−7.6	>120	199.3	
6	N8 C8 AR1 B23	2.″87	−0.″03	15.75	12.05	10.37	−7.6	>120	166.3	
7	N10 C5 AR4 B21	3.″53	2.″73	15.74	12.16	10.48	−7.5	>120	150.2	
8	N7 C6 AR2 B24	2.″46	1.″01	16.31	12.54	10.76	−7.3	>120	206.0	
9	N5 C1	0.″80	10.″50	16.10	12.44	10.77	−7.3	>120	106.7	
10	B30	−1.″83	−4.″25	17.37	13.35	11.46	−7.1	>120	51.8	
11	···	−1.″03	14.″41	17.02	12.72	10.92	−7.1	>120	···	
12	N6 C3 AR16 B25	1.″01	4.″98	16.40	12.67	10.99	−7.0	>120	162.7	
13	B31	−2.″08	−1.″39	17.59	13.63	11.74	−6.9	116.9	18.2	
14	B12	6.″24	−0.″32	16.38	12.84	11.22	−6.7	106.3	124.9	
15	N12 CB B8	7.″24	5.″67	16.12	12.78	11.27	−6.5	99.7	41.2	
16	B19	4.″22	1.″59	16.62	13.01	11.40	−6.5	99.5	97.5	
17	B29	−0.″89	−4.″90	18.13	14.05	12.15	−6.5	97.6	47.1	
18	AR9 B20	3.″58	4.″34	16.70	13.17	11.63	−6.2	92.0	17.6	
19	AR6	−5.″81	−3.″72	18.89	14.58	12.60	−6.2	92.0	0.6	
20	···	2.″90	2.″58	17.49	13.88	12.16	−6.1	89.1	1.6	
21	B7	7.″36	2.″65	16.85	13.29	11.77	−6.1	87.8	17.2	
22	B27	0.″24	5.″55	17.46	13.65	12.02	−6.1	87.7	11.4	
23	B2	12.″50	−1.″08	17.56	13.82	12.19	−5.9	70.3	11.4	
24	···	−1.″42	1.″55	18.27	14.40	12.61	−5.8	66.7	1.4	
25	···	−3.″26	−4.″30	19.42	15.05	13.05	−5.8	66.1	10.9	
26	B18	4.″60	−1.″27	17.70	13.98	12.34	−5.8	64.9	−0.7	
27	B16	5.″31	2.″74	17.13	13.49	12.01	−5.7	63.0	22.1	
28	B14	5.″77	0.″55	17.26	13.69	12.17	−5.7	61.7	6.7	
29	B9	7.″08	4.″62	17.23	13.81	12.26	−5.7	61.0	3.5	

Table 3—Continued

ID[a]	Desig./Ref.[b]	ΔRA[c]	ΔDEC[c]	m_{F110W}	m_{F160W}	m_{F205W}	M_K[d]	M_{init}[e]	EW[f]	
		″	″	mag.	mag.	mag.	mag.	$M_\odot$	Å	$ergs$
(1)	(2)	(3)	(4)	(5)	(6)	(7)	(8)	(9)	(10)	
30	···	0.″20	3.″66	17.87	14.16	12.53	−5.6	59.0	1.5	
31	···	2.″87	2.″60	17.70	13.97	12.41	−5.5	58.7	1.6	
32	B15	5.″53	2.″41	17.59	13.96	12.42	−5.5	57.6	8.7	
33	B13	6.″08	2.″36	17.53	13.95	12.42	−5.4	57.0	23.2	
34	B5	7.″93	1.″22	17.67	14.03	12.49	−5.4	56.6	6.3	
35	B10	6.″51	5.″26	17.29	13.84	12.37	−5.4	56.1	8.4	
36	···	−6.″19	14.″87	19.03	14.53	12.60	−5.4	56.0	···	
37	N10 C5 AR4 B21	3.″54	2.″99	99.00	14.55	12.63	−5.3	55.5	46.3	
38	B11	6.″51	2.″28	17.51	13.85	12.38	−5.3	55.3	38.6	
39	···	11.″91	−13.″94	18.10	14.37	12.65	−5.3	55.2	···	
40	···	5.″59	3.″93	17.78	14.24	12.67	−5.3	54.7	10.7	
41	···	2.″22	−4.″66	19.53	15.47	13.53	−5.2	53.5	6.6	
42	···	1.″37	1.″52	18.02	14.41	12.82	−5.2	53.0	2.2	
43	···	3.″76	3.″59	18.45	14.69	13.04	−5.1	51.9	−3.7	
44	···	5.″80	−2.″83	18.25	14.47	12.88	−5.1	51.9	1.2	
45	···	3.″11	−1.″49	18.47	14.64	13.01	−5.1	50.9	6.8	
46	···	11.″18	−5.″42	19.03	14.69	12.90	−5.1	50.6	···	
47	···	6.″49	−2.″52	18.01	14.46	12.90	−5.0	50.2	5.0	
48	···	4.″77	−4.″20	18.73	15.00	13.28	−5.0	50.2	−3.2	
49	···	−1.″74	14.″97	18.36	14.59	12.94	−5.0	49.9	···	
50	···	−1.″65	−3.″41	19.57	15.38	13.53	−5.0	49.9	2.1	
51	···	10.″80	−1.″62	19.82	14.99	12.94	−5.0	49.9	−7.8	
52	···	12.″43	−10.″55	18.59	14.67	12.94	−5.0	49.9	···	
53	···	5.″96	−2.″25	18.25	14.51	12.94	−5.0	49.7	6.4	
54	···	0.″14	6.″95	18.77	14.78	13.02	−5.0	48.4	−5.4	
55	···	6.″93	0.″15	18.13	14.57	13.03	−4.9	48.1	−10.4	
56	···	4.″35	0.″57	18.15	14.54	13.03	−4.9	48.1	−11.4	
57	B11	6.″67	2.″45	18.01	14.53	13.04	−4.9	47.9	···	
58	···	−3.″84	3.″16	18.87	14.90	13.05	−4.9	47.8	−8.7	

Table 3—Continued

ID[a]	Desig./Ref.[b]	ΔRA[c]	ΔDEC[c]	m_{F110W}	m_{F160W}	m_{F205W}	M_K[d]	M_{init}[e]	EW[f]	F_{F190}
		″	″	mag.	mag.	mag.	mag.	$M_\odot$	Å	$ergs\ cm^{-2}$
(1)	(2)	(3)	(4)	(5)	(6)	(7)	(8)	(9)	(10)	(11)
59	···	11.″54	8.″42	18.27	14.63	13.05	−4.9	47.8	···	
60	···	7.″08	0.″58	18.32	14.56	13.02	−4.9	47.0	7.0	3.
61	···	−1.″53	23.″67	18.56	14.69	13.09	−4.9	47.0	···	
62	···	2.″20	6.″15	18.10	14.57	13.04	−4.8	46.4	−0.5	2.
63	···	7.″60	−2.″92	18.21	14.64	13.15	−4.8	46.0	−22.0	2.
64	···	2.″91	6.″05	18.25	14.69	13.13	−4.8	45.9	0.7	2.
65	···	−2.″34	1.″23	18.67	14.90	13.16	−4.8	45.7	−5.6	2.
66	···	3.″57	2.″34	18.32	14.63	13.11	−4.8	44.9	−1.4	2.
67	···	2.″82	7.″66	18.68	14.94	13.35	−4.7	43.8	−4.2	2.
68	···	7.″82	4.″61	17.74	14.33	12.93	−4.7	43.7	−5.1	3.
69	···	7.″72	2.″44	18.10	14.52	13.06	−4.7	43.5	−0.4	3.
70	···	−0.″10	−0.″63	18.89	14.94	13.30	−4.7	43.2	−9.4	2.
71	···	−2.″63	6.″33	19.28	15.32	13.62	−4.7	43.1	−3.7	1.
72	···	6.″88	2.″49	18.21	14.62	13.13	−4.6	42.5	32.1	2.
73	···	5.″50	−2.″82	18.81	14.96	13.35	−4.6	42.3	−12.4	2.
74	···	9.″63	−4.″73	18.73	14.98	13.36	−4.6	42.2	···	
75	···	7.″42	11.″51	19.83	15.32	13.36	−4.6	42.2	···	
76	···	1.″07	5.″70	18.81	14.98	13.38	−4.6	41.9	−14.2	2.
77	···	6.″71	2.″93	18.40	14.74	13.25	−4.6	41.3	−1.4	2.
78	···	22.″07	−1.″95	19.03	15.08	13.44	−4.5	40.8	···	
79	···	−2.″45	4.″65	19.91	15.41	13.46	−4.5	40.5	−9.4	1.
80	···	4.″33	3.″30	18.45	14.92	13.47	−4.5	40.3	−5.2	2.
81	···	5.″95	−1.″48	18.74	15.02	13.48	−4.5	40.1	−10.9	2.
82	···	6.″26	3.″63	18.35	14.93	13.40	−4.5	40.1	−2.2	2.
83	···	−2.″62	2.″09	19.21	15.34	13.53	−4.4	39.3	−9.4	1.
84	···	3.″50	6.″48	18.70	15.08	13.54	−4.4	39.1	−13.6	1.
85	···	2.″94	4.″16	18.50	15.03	13.54	−4.4	39.1	−8.8	1.
86	···	9.″53	−10.″83	18.33	15.00	13.56	−4.4	38.7	···	
87	···	3.″39	6.″18	18.71	15.10	13.60	−4.4	38.1	−5.4	1.

Table 3—Continued

ID[a]	Desig./Ref.[b]	ΔRA[c]	ΔDEC[c]	m_{F110W}	m_{F160W}	m_{F205W}	M_K[d]	M_{init}[e]	EW[f]	F_{F1}
		″	″	mag.	mag.	mag.	mag.	$M_\odot$	Å	$ergs\ cm^-$
(1)	(2)	(3)	(4)	(5)	(6)	(7)	(8)	(9)	(10)	(11
88	···	−7.″98	5.″53	20.11	15.55	13.62	−4.3	37.8	···	
89	···	9.″14	5.″61	18.48	15.07	13.65	−4.3	37.3	−7.1	
90	···	4.″08	−10.″21	19.37	15.38	13.68	−4.3	36.9	−20.6	
91	···	−3.″70	5.″24	19.36	15.52	13.69	−4.3	36.8	−6.8	
92	···	3.″39	1.″31	18.59	14.95	13.48	−4.3	36.8	−2.9	
93	···	1.″52	−0.″02	19.18	15.43	13.81	−4.3	36.5	0.4	
94	···	5.″22	−5.″27	19.81	15.91	14.14	−4.3	36.5	−1.1	
95	···	4.″18	0.″76	18.73	15.18	13.71	−4.3	36.4	−8.5	
96	···	6.″10	3.″03	18.47	15.01	13.54	−4.3	36.3	−5.3	
97	···	14.″78	6.″19	19.02	15.33	13.73	−4.2	36.2	···	
98	···	11.″74	−14.″30	19.16	15.36	13.75	−4.2	35.8	···	
99	···	4.″01	5.″67	19.42	15.35	13.76	−4.2	35.6	−47.3	
100	···	10.″53	5.″15	18.71	15.21	13.77	−4.2	35.6	···	
101	···	8.″59	4.″39	18.69	15.28	13.78	−4.2	35.4	−10.0	
102	···	8.″09	−6.″04	19.19	15.35	13.78	−4.2	35.4	−9.7	
103	···	−7.″64	0.″18	21.30	16.45	14.53	−4.2	35.3	3.0	
104	···	4.″17	−21.″01	19.13	15.39	13.79	−4.2	35.3	···	
105	···	4.″41	−16.″84	20.07	15.71	13.81	−4.2	34.9	···	
106	···	−4.″92	−0.″47	99.00	15.47	13.82	−4.1	34.8	−169.5	
107	···	−5.″10	−8.″23	19.11	15.39	13.87	−4.1	34.1	···	
108	···	7.″22	11.″83	19.29	15.54	13.89	−4.1	33.7	···	
109	···	3.″42	2.″06	19.19	15.44	13.91	−4.1	33.5	−10.2	
110	···	4.″13	6.″41	19.04	15.44	13.93	−4.0	33.2	−11.2	
111	···	0.″65	18.″90	19.47	15.67	13.94	−4.0	33.1	···	
112	···	3.″25	6.″40	18.94	15.40	13.87	−4.0	32.9	−0.3	
113	···	−3.″19	5.″29	19.80	15.70	13.97	−4.0	32.7	−8.0	
114	···	7.″15	3.″69	18.97	15.46	13.99	−4.0	32.3	−6.3	
115	···	2.″32	2.″72	19.27	15.32	13.83	−4.0	32.3	2.9	
116	···	3.″64	16.″48	19.53	15.71	14.01	−4.0	32.1	···	

Table 3—Continued

ID[a]	Desig./Ref.[b]	ΔRA[c]	ΔDEC[c]	m_{F110W}	m_{F160W}	m_{F205W}	M_K[d]	M_{init}[e]	EW[f]	F_{F19}
		″	″	mag.	mag.	mag.	mag.	$M_\odot$	$\AA$	$ergs\ cm^-$
(1)	(2)	(3)	(4)	(5)	(6)	(7)	(8)	(9)	(10)	(11
117	···	6.″51	3.″32	19.14	15.54	14.06	−3.9	31.4	−8.0	
118	···	2.″54	−3.″21	19.66	15.82	14.08	−3.9	31.1	−8.0	
119	···	7.″65	0.″01	19.29	15.62	14.06	−3.9	31.1	0.2	
120	···	5.″68	−7.″20	19.82	15.86	14.09	−3.9	31.1	−14.9	
121	···	−0.″73	3.″12	19.51	15.66	14.09	−3.9	31.0	−11.4	
122	···	1.″29	5.″48	19.24	15.58	14.09	−3.9	30.9	−13.6	
123	B14	5.″58	0.″41	99.00	15.96	14.11	−3.9	30.8	−16.8	
124	···	6.″02	5.″50	19.49	15.66	14.11	−3.9	30.7	−8.5	
125	···	16.″14	1.″01	20.41	16.03	14.15	−3.8	30.1	···	
126	···	8.″80	19.″13	19.12	15.73	14.16	−3.8	30.0	···	
127	···	12.″14	−8.″76	20.41	15.98	14.16	−3.8	30.0	···	
128	···	12.″56	−13.″77	19.69	15.86	14.18	−3.8	29.8	···	
129	···	−9.″61	10.″04	20.61	16.16	14.20	−3.8	29.4	···	
130	···	4.″53	−4.″74	19.94	15.97	14.21	−3.8	29.3	−12.9	
131	B29	−1.″28	−4.″70	20.04	16.01	14.23	−3.7	29.1	−17.2	
132	···	7.″04	20.″08	19.61	15.90	14.27	−3.7	28.5	···	
133	···	6.″72	7.″79	19.25	15.90	14.27	−3.7	28.5	−14.2	
134	···	3.″14	−13.″78	20.15	16.18	14.28	−3.7	28.4	···	
135	···	1.″35	−2.″97	19.91	16.06	14.29	−3.7	28.3	−13.2	
136	···	−2.″41	−5.″08	20.53	16.21	14.30	−3.7	28.1	−6.4	
137	···	16.″11	1.″50	20.92	16.32	14.32	−3.7	27.9	···	
138	···	−0.″63	−16.″45	20.61	16.37	14.35	−3.6	27.5	···	
139	···	12.″45	−0.″65	19.75	15.96	14.36	−3.6	27.3	−10.7	
140	···	3.″99	4.″28	19.19	15.83	14.38	−3.6	27.2	−9.9	
141	···	−18.″83	3.″95	20.93	16.41	14.39	−3.6	26.9	···	
142	···	5.″64	−2.″17	19.76	15.97	14.41	−3.6	26.7	···	
143	···	5.″99	5.″52	19.69	16.02	14.43	−3.5	26.5	−8.5	
144	···	16.″64	2.″18	20.22	16.19	14.43	−3.5	26.5	···	
145	···	15.″57	2.″69	19.65	16.05	14.44	−3.5	26.3	···	

Table 3—Continued

ID[a]	Desig./Ref.[b]	ΔRA[c]	ΔDEC[c]	m_{F110W}	m_{F160W}	m_{F205W}	M_K[d]	M_{init}[e]	EW[f]	F_{F19}
		″	″	mag.	mag.	mag.	mag.	$M_\odot$	$\AA$	$ergs\ cm^-$
(1)	(2)	(3)	(4)	(5)	(6)	(7)	(8)	(9)	(10)	(11
146	···	−5.″16	7.″86	19.96	16.07	14.45	−3.5	26.2	−9.7	
147	···	14.″38	2.″76	19.63	16.11	14.46	−3.5	26.2	···	
148	···	20.″04	−5.″66	19.69	16.07	14.47	−3.5	26.0	···	
149	···	5.″54	21.″20	20.39	16.16	14.47	−3.5	26.0	···	
150	···	2.″57	3.″12	19.57	15.81	14.31	−3.5	25.9	12.8	
151	···	7.″48	−4.″87	19.91	16.09	14.48	−3.5	25.9	···	
152	···	5.″71	−13.″80	20.25	16.28	14.48	−3.5	25.8	···	
153	···	1.″31	2.″76	20.15	16.12	14.51	−3.5	25.5	−5.7	
154	···	−3.″52	−10.″44	20.43	16.34	14.52	−3.5	25.4	···	
155	···	2.″13	3.″63	19.74	16.00	14.52	−3.4	25.4	−12.2	
156	···	5.″02	20.″61	20.38	16.30	14.54	−3.4	25.2	···	
157	···	−0.″53	−1.″42	20.12	16.33	14.55	−3.4	25.0	−15.2	
158	···	10.″98	0.″77	99.00	16.33	14.56	−3.4	24.9	−5.2	
159	···	8.″17	7.″07	20.43	16.32	14.57	−3.4	24.8	···	
160	···	3.″16	6.″95	19.81	16.11	14.59	−3.4	24.6	−12.4	
161	···	8.″35	−17.″92	20.86	16.48	14.59	−3.4	24.6	···	
162	···	7.″36	−16.″34	20.12	16.27	14.59	−3.4	24.6	···	
163	···	2.″31	−0.″64	20.01	16.17	14.60	−3.4	24.5	4.2	
164	···	7.″91	14.″29	19.75	16.15	14.61	−3.4	24.4	···	
165	···	11.″83	7.″40	19.62	16.14	14.65	−3.3	23.9	···	
166	···	5.″46	3.″19	19.80	16.20	14.69	−3.3	23.5	−10.4	
167	···	6.″22	5.″03	19.34	15.86	14.42	−3.3	23.4	9.8	
168	···	3.″09	−7.″45	20.48	16.55	14.70	−3.3	23.4	−13.4	
169	···	1.″54	2.″50	20.09	16.32	14.72	−3.3	23.3	−6.3	
170	AR11	5.″83	1.″80	19.87	16.16	14.74	−3.2	23.1	−12.2	
171	···	−12.″94	10.″63	20.39	16.48	14.76	−3.2	22.8	···	
172	···	−0.″37	5.″24	20.22	16.31	14.76	−3.2	22.8	−4.7	
173	···	−0.″74	2.″52	20.13	16.30	14.80	−3.2	22.5	−15.9	
174	···	6.″38	−5.″44	20.30	16.53	14.81	−3.2	22.4	−9.2	

Table 3—Continued

ID[a]	Desig./Ref.[b]	ΔRA[c]	ΔDEC[c]	m_{F110W}	m_{F160W}	m_{F205W}	M_K[d]	M_{init}[e]	EW[f]	F_{F190}
		″	″	mag.	mag.	mag.	mag.	$M_\odot$	$\AA$	$ergs\ cm^{-2}$
(1)	(2)	(3)	(4)	(5)	(6)	(7)	(8)	(9)	(10)	(11)
175	···	2.″67	19.″47	20.65	16.56	14.82	−3.1	22.2	···	
176	···	0.″30	−1.″09	20.34	16.66	14.83	−3.1	22.1	−13.4	5.
177	···	4.″52	5.″89	20.07	16.31	14.83	−3.1	22.1	−7.8	5.
178	···	7.″41	15.″81	21.14	16.69	14.85	−3.1	22.0	···	
179	···	14.″40	1.″39	20.64	16.53	14.85	−3.1	21.9	···	
180	···	0.″31	23.″12	20.77	16.65	14.89	−3.1	21.6	···	
181	···	4.″04	15.″06	20.08	16.43	14.90	−3.1	21.4	···	
182	···	4.″29	−0.″15	19.92	16.17	14.70	−3.1	21.3	7.8	6.
183	···	−5.″10	−19.″55	21.11	16.74	14.93	−3.0	21.2	···	
184	···	−3.″31	−6.″67	21.23	16.90	14.94	−3.0	21.0	−11.0	4.
185	···	0.″29	−4.″80	20.71	16.65	14.95	−3.0	20.9	−10.4	5.
186	···	−3.″40	−5.″48	21.36	16.91	14.95	−3.0	20.9	−18.3	4.
187	···	3.″71	−0.″54	20.14	16.42	14.96	−3.0	20.8	6.6	5.
188	···	8.″89	0.″96	20.15	16.49	14.97	−3.0	20.7	−9.4	4.
189	···	4.″40	−0.″76	19.90	16.24	14.77	−3.0	20.7	4.0	5.
190	···	−6.″58	3.″00	20.61	16.72	14.99	−3.0	20.6	−18.3	4.
191	···	11.″56	4.″59	20.03	16.51	15.00	−3.0	20.5	···	
192	···	−2.″78	17.″82	20.57	16.66	15.00	−3.0	20.4	···	
193	···	1.″61	13.″20	20.32	16.60	15.00	−3.0	20.4	−4.7	4.
194	···	3.″56	14.″83	21.41	16.96	15.01	−3.0	20.3	···	
195	···	3.″55	7.″46	20.13	16.48	15.03	−2.9	20.1	−8.0	4.
196	···	2.″67	15.″02	20.54	16.69	15.03	−2.9	20.1	···	

[a]ID numbers were assigned by sorting the data in order of increasing M_K (decreasing luminosity), and stars outside the range $1.4 < m_{160} - m_{205} < 2.1$

[b]Designations are taken from the following, in order of preference: (1) Nagata et al. (1995) (N#), (2) C al. (1996) (C#), (3) Lang et al. (2001) (AR#), and (4) Blum et al. (2001) (B#). Radio sources AR9-17 a identified in this paper, and their coordinates have been extracted from Figure 2 of Lang et al. (2001).

[c]Positions are with respect to RA(J2000) $17^h\ 45^m\ 50.26^s$ DEC(J2000) $-28°\ 49'\ 22.''76$ and have a relat of $\pm 0.008''$.

[d]M_K assumes $(m_{205}\text{-K})_0=0$, d=8000 pc (Reid 1993), $(m_{160} - m_{205})_0=-0.05$ and $A_K = 1.95 \times E(H-K)$

[e]$M_{\rm initial}$ assumes the relation between mass and magnitude for τ=2.5 *Myr* from the Geneva models w metallicity and enhanced mass-loss rates.

[f]Equivalent is calculated as $EW = [(F_{\rm F187N} - F_{\rm F190N})/F_{\rm F190N}] * \Delta\lambda_{\rm F187N}$, where $F_{\rm F187N}$ is corrected for e and the intrinsic shape of the spectral energy distribution.

Table 4. Model Parameters

star#	#8	#10$_a$	#10$_b$	#10$_c$
log L$_*$/$L_\odot$	6.26	6.27	6.15	6.24
R$_*$/$R_\odot$	43.5	46.8	46.8	46.8
T$_*$ kK	32.2	31.1	29.1	30.7
R$_{\tau=2/3}$/$R_\odot$	47.5	48.2	48.6	48.2
T$_{\rm eff}$ kK	30.9	30.7	28.5	30.3
v_∞km s^{-1}	1100	1000:	1000:	1600:
log $\dot{M}/M_\odot\ yr^{-1}$	−4.35	−5.37	−4.79	−5.21
β	1.25	2.25	1.50	2.25
f	0.1	0.1	1.0	.1
m$_{\rm F205W}$	10.71	11.44	11.45	11.43
m$_{\rm F160W}$	12.50	13.33	13.35	13.32
m$_{\rm F110W}$	16.27	17.41	17.43	17.40
EW$_{\rm P\alpha}$ $\mathring{A}$	242.	54.0	63.3	54.9
A$_{\rm k}$	3.34	3.80	3.75	3.75
H[a]	0.27	0.42	0.42	0.42
He[a]	0.71	0.56	0.56	0.56
C[a]	0.0002:	0.0008:	0.0008:	0.0008:
N[a]	0.016	0.006:	0.006:	0.006:
log Q(H$^+$)	49.9	49.8	49.5	49.7
log Q(He$^+$)	48.5	48.4	47.6	48.2

[a]Mass fraction

Note. — Quantities followed by a colon are upper limits.

REFERENCES

Bieging, J. H., Abbott, D. C., & Churchwell, E. B. 1982, ApJ, 263, 207

Blum, R. D., Schaerer, D., Pasquali, A., Heydari-Malayeri, M., Conti, P. S., Schmutz, W. 2001, AJ, accepted

Bohannan, B., & Crowther, P.A., 1999, ApJ, 511, 374

Brown, R. L. & Liszt, H. S. 1984, ARA&A, 22, 223

Cantó, J., Raga, A. C., & Rodríguez, L. F. 2000, ApJ, 536, 896

Colgan, S. W. J., Erickson, E. F., Simpson, J. P., Haas, M. R., & Morris, M. 1996, ApJ, 470, 882

Conti, P. S., Hanson, M. M., Morris, P. W., Willis, A. J., & Fossey, S. J. 1995, ApJ, 445, L35

Cotera, A. S., Erickson, E. F., Simpson, J. P., Colgan, S. W. J., Allen, D. A., & Burton, M. G. 1992, American Astronomical Society Meeting, 181, 8702

Cotera, A. S. 1995, Ph.D. Thesis, Stanford University

Cotera, A. S., Erickson, E. F., Colgan, S. W. J., Simpson, J. P., Allen, D. A., & Burton, M. G. 1996, ApJ, 461, 750

Crowther, P. A. & Dessart, L. 1998, MNRAS, 296, 622

Davidson, J. A., Morris, M., Harvey, P. M., Lester, D. F., Smith, B., & Werner, M. W. 1994, NATO ASIC Proc. 445: The Nuclei of Normal Galaxies: Lessons from the Galactic Center, 231

Eckart, A., Ott, T., & Genzel, R. 1999, A&A, submitted

Erickson, E. F., Colgan, S. W. J., Simpson, J. P., Rubin, R. H., Morris, M., & Haas, M. R. 1991, ApJ, 370, L69

Figer, D. F., Najarro, F., Morris, M., McLean, I. S., Geballe, T. R., Ghez, A. M., & Langer, N. 1998, ApJ, 506, 384

Figer, D. F. et al. 2000a, ApJ, 533, L49

Figer, D. F., McLean, I. S., Becklin, E. E., Graham, J. R., Larkin, J. E., Levenson, N. A., & Teplitz, H. I. 2000b, Proc. SPIE, 4005, 104

Figer, D. F., McLean, I. S., & Najarro, F. 1997, ApJ, 486, 420

Figer, D. F., McLean, I. S., & Morris, M. 1995, ApJ, 447, L29

Figer, D. F. 1995, Ph.D. Thesis, University of California, LosAngeles

Figer, D. F., Kim, S. S., Morris, M., Serabyn, E., Rich, R. M., & McLean, I. S. 1999a, ApJ, 525, 750

Figer, D. F., Morris, M., Geballe, T. R., Rich, R. M., Serabyn, E., McLean, I. S., Puetter, R. C., & Yahil, A. 1999b, ApJ, 525, 759

Figer, D. F., et al. 2002, in preparation

Genzel, R. et al. 1990, ApJ, 356, 160

Gerhard, O. 2001, ApJ, 546, L39

Hanson, M. M., Conti, P. S., & Rieke, M. J. 1996, ApJS, 107, 281

Herald, J.E., Hillier, D. J. & Schulte-Ladbeck, R.E. 2001, ApJ, 548, 932

Hillier, D. J. 1989, ApJ, 347, 392

Hillier, D. J. & Miller, D. L. 1998, ApJ, 496, 407

Hillier, D. J. & Miller, D. L. 1999, ApJ, 519, 354

Ho, L. C. & Filippenko, A. V. 1996, ApJ, 466, L83

Illingworth, G. 1976, ApJ, 204, 73

Keyes, T., et al. 1997, HST Data Handbook, Ver. 3.0, Vol. I (Baltimore: STScI)

Krabbe, A., et al., ApJ, 447, L95

Kim, S. S., Morris, M., & Lee, H. M. 1999, ApJ, 525, 228

Kim, S. S., Figer, D. F., Lee, H. M., & Morris, M. 2000, ApJ, 545, 301

Kim, S. S., & Morris, M. 2002, in preparation

Kurucz, R. L. 1979, ApJS, 40, 1

Lang, C. C., Goss, W. M., & Wood, D. O. S. 1997, ApJ, 481, 1016

Lang, C. C., Goss, W. M., & Rodríguez, L. F. 2001a, ApJ, 551, L143

Lang, C. C., Goss, W. M., & Morris, M. 2001b, AJ, 121, 2681

Leitherer, C., Chapman, J. M., & Koribalski, B. 1997, ApJ, 481, 898

McGinn, M. T., Sellgren, K., Becklin, E. E., & Hall, D. N. B. 1989, ApJ, 338, 824

McLean et al. 1998, SPIE Vol. 3354, 566

McLean et al. 2002, PASP, in preparation

Meynet, G., Maeder, A., Schaller, G., Schaerer, D., & Charbonnel, C. 1994, A&A Supp., 103, 97

Meynet, G. 1995, A&A, 298, 767

Mizutani, K. et al. 1994, ApJS, 91, 613

Moneti, A., Glass, I. S. & Moorwood, A. F. M. 1994, MNRAS, 268, 194

Morris, M. & Yusef-Zadeh, F. 1989, ApJ, 343, 703

Morris, M., Davidson, J. A., & Werner, M. W. 1995, ASP Conf. Ser. 73: From Gas to Stars to Dust, 477

Najarro, F. et al. 2002, in preparation

Nagata, T., Woodward, C. E., Shure, M., & Kobayashi, N. 1995, AJ, 109, 1676

Nugis, T., Crowther, P. A., & Willis, A. J. 1998, A&A, 333, 956

Ozernoy, L. M., Genzel, R., & Usov, V. V. 1997, MNRAS, 288, 237

Perryman, M. A. C. et al. 1997, A&A, 323, L49

Portegies-Zwart, S. F., Makino, J., McMillan, S. L. W., & Hut, P. 2001, ApJ, 546, L101

Reid, M. J. 1993, ARA&A, 31, 345

Rieke, G. H., Rieke, M. J., & Paul, A. E. 1989, ApJ, 336, 752

Salpeter, E. E. 1955, ApJ, 121, 161

Scalo, J. 1998, in *The Stellar Initial Mass Function*, G. Gilmore and D. Howell (eds.), vol. 142 of 38^{th} *Herstmonceux Conference*, San Francisco, ASP Conference Series, p. 201

Schaller, G., Schaerer, D., Meynet, G., & Maeder, A. 1992, A&AS, 96, 269

Serabyn, E. & Guesten, R. 1987, A&A, 184, 133

Serabyn, E., Shupe, D., & Figer, D. F. 1998, Nature, 394, 448

Serabyn, E., Shupe, D., & Figer, D. F. 1999, ASP Conf. Ser. 186: The Central Parsecs of the Galaxy, 320

Serabyn, E., Figer, D. F., Kim, S. S., Morris, M., & Rich, R. M. 2002, ApJ, in preparation

Stetson, P. 1987, PASP, 99, 191

Stolte, A., Grebel, E. K., Brandner, W., & Figer, D. F. 2002, å, submitted

Timmermann, R., Genzel, R., Poglitsch, A., Lutz, D., Madden, S. C., Nikola, T., Geis, N., & Townes, C. H. 1996, ApJ, 466, 242

van der Hucht, K. A. 2001, New Astronomy Review, 45, 135

Wendker, H. J. 1995, A&AS, 109, 177

Yusef-Zadeh, F., Cotera, A., Fruscione, A., Lang, C., Law, C., Wang, D., & Wardle, M. 2001, American Astronomical Society Meeting, 198, 8709

Yusef-Zadeh, F., Law, C., Wardle, M., Wang, Q. D., Fruscione, A., Lang, C. C., & Cotera, A. 2002, in preparation

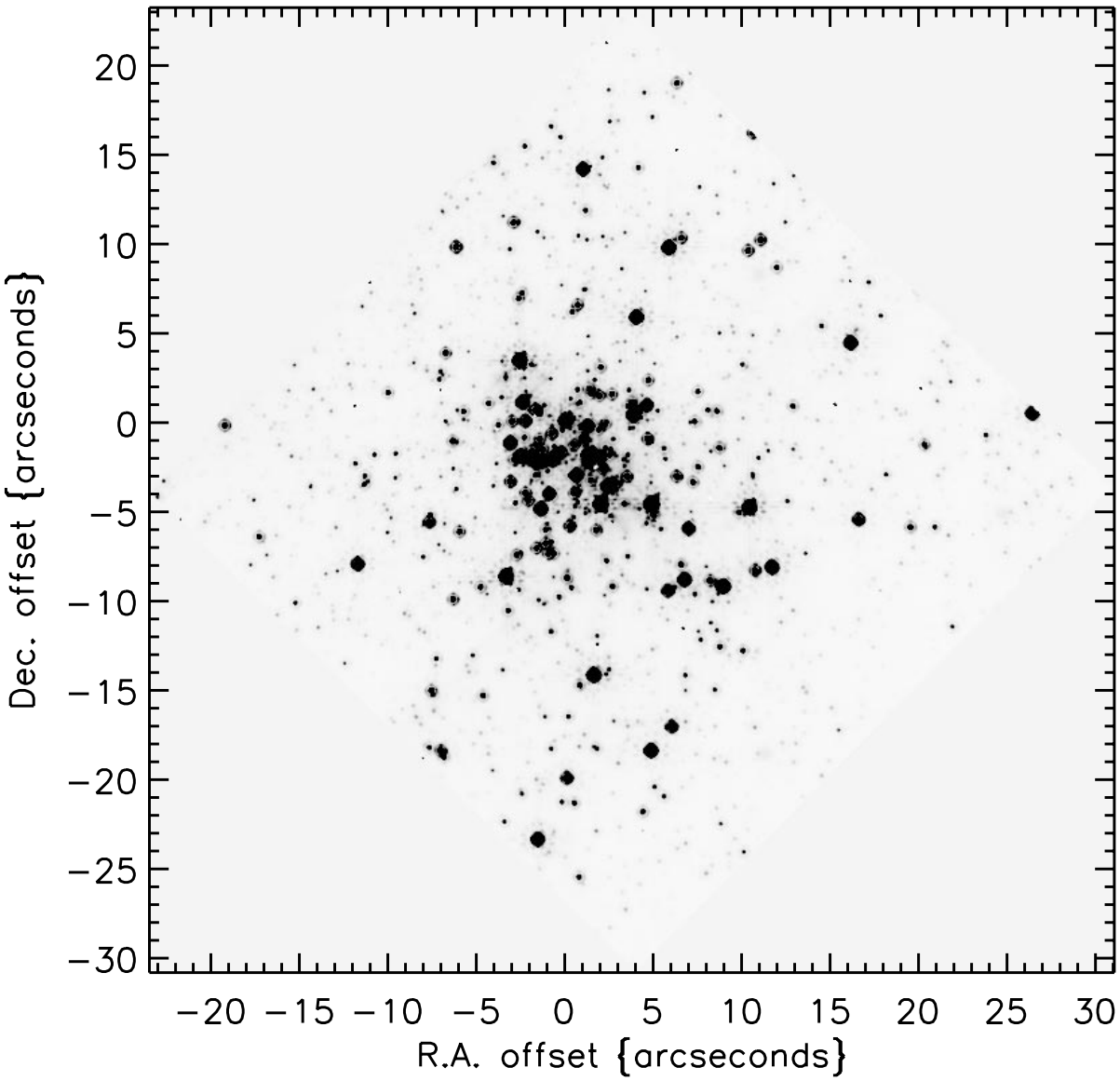

Fig. 1a.— *(a)* F205W image, after processing by calnica and calnicb.

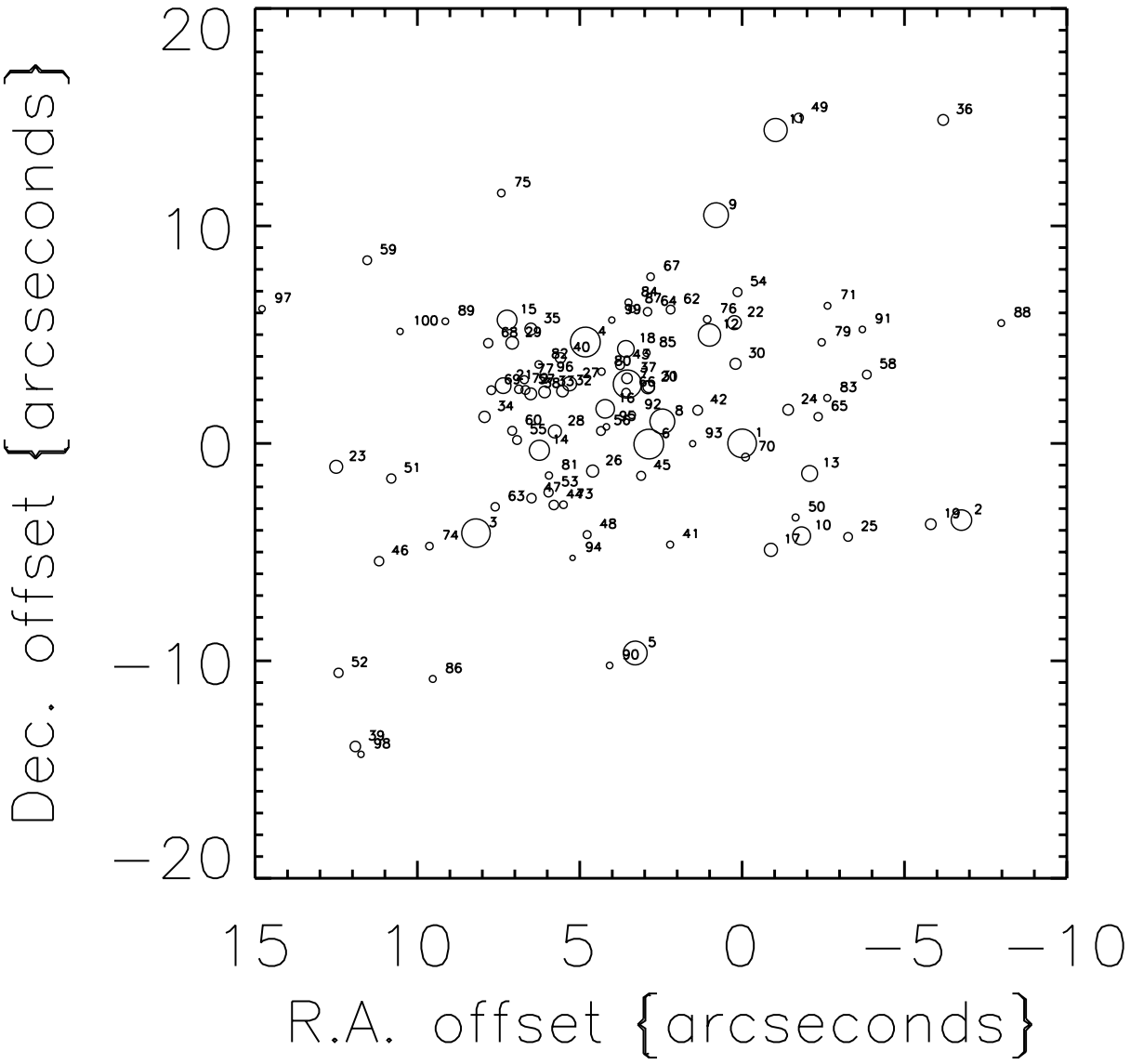

Fig. 1b.— *(b)* ID's of bright stars.

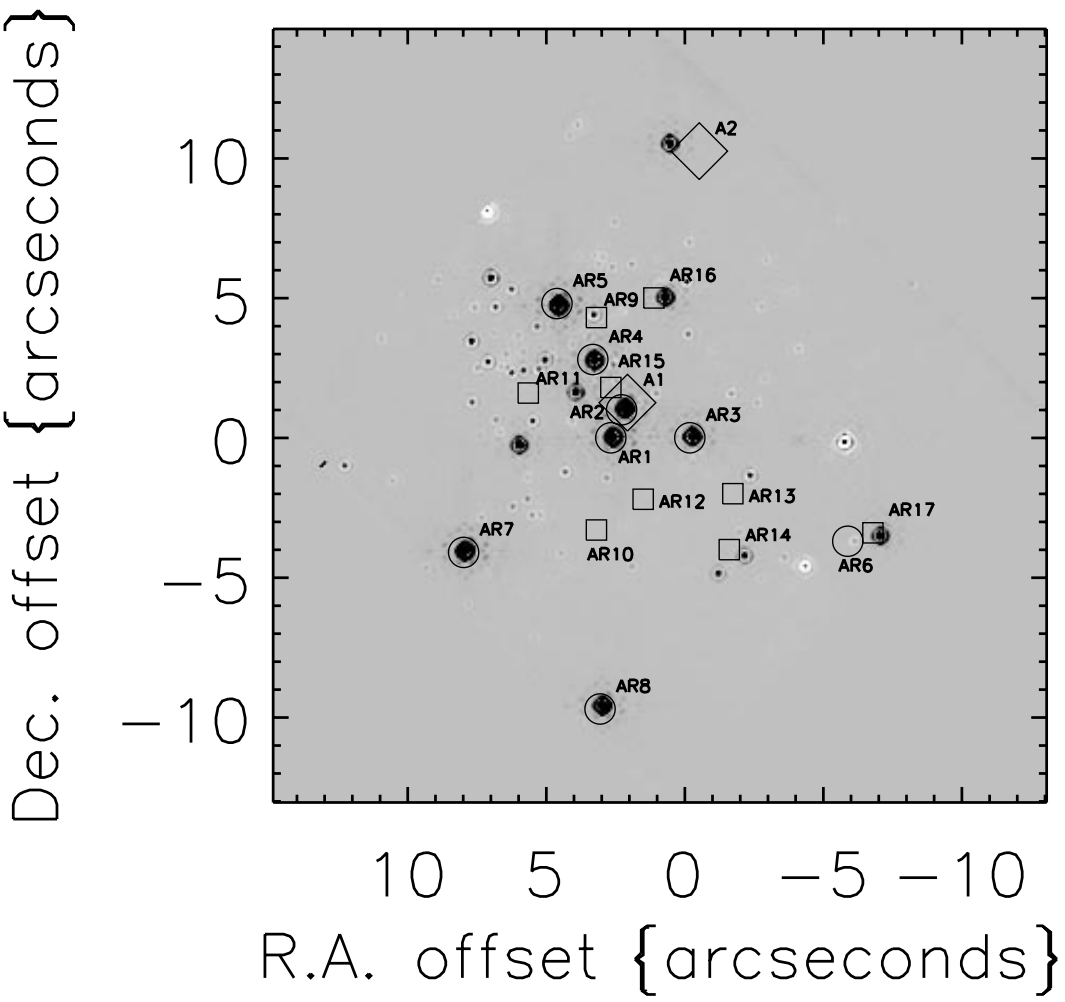

Fig. 2.— Difference image made by subtracting F190N image from F187N image. Positions of radio sources AR1−8 (*circles*) are from Lang, Goss, & Rodríguez (2001a). Radio sources AR9−17 (*squares*) are newly identified in this paper, and their coordinates are taken from Figure 2 in Lang, Goss, & Rodríguez (2001a). Positions of x-ray sources (*diamonds*) are from Yusef-Zadeh et al. (2002).

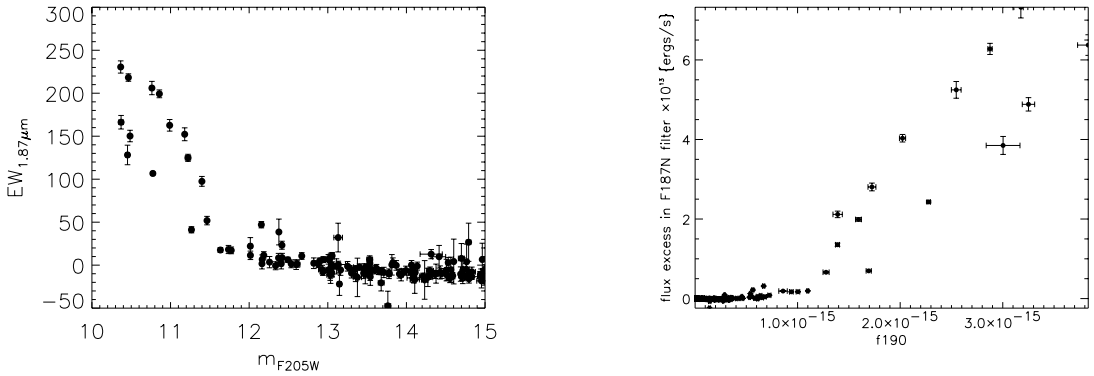

Fig. 3.— *(a)* Plot of $EW_{1.87}\ \mu m$ as a function of $m_{\rm F205W}$. *(b)* Linear plot of excess flux in F187N versus $F_{\rm F190N}$.

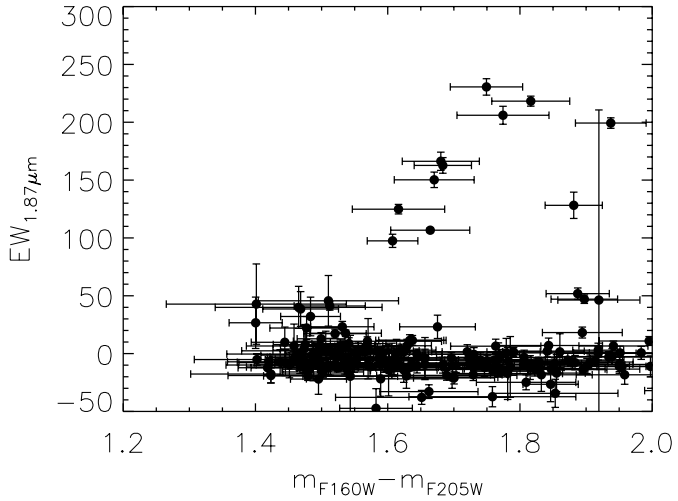

Fig. 4.— Plot of $EW_{1.87}\ \mu m$ as a function of color in $m_{\rm F160W}-m_{\rm F205W}$. The plot includes data points where the color error is less than 0.2.

Fig. 5a.— Spectra of selected stars from Table 3. The spectra have not been dereddened, and the flux scale is arbitrary. The wavelength gaps in the spectra are due to incomplete coverage of the cross-dispersed echelle format by the detector. The two sharp absorption features near 2.32 μm are due to imperfect correction for telluric absorption. Other sharp features (a few pixels wide), especially in the left-most order, are similarly due to this imperfect correction, or are due to detector artifacts, c.f. the feature near 2.294 μm in the spectrum of star #2.

Fig. 5b.— Same as Figure 5a.

Fig. 5c.— Same as Figure 5a. The sharp features near 2.294 μm in the spectra of star #10 and #14 are due to detector artifacts.

Fig. 5d.— Same as Figure 5a.

Fig. 5e.— Same as Figure 5a.

Fig. 5f.— Same as Figure 5a.

Fig. 5g.— Same as Figure 5a.

Fig. 5h.— Same as Figure 5a.

Fig. 5i.— Same as Figure 5a.

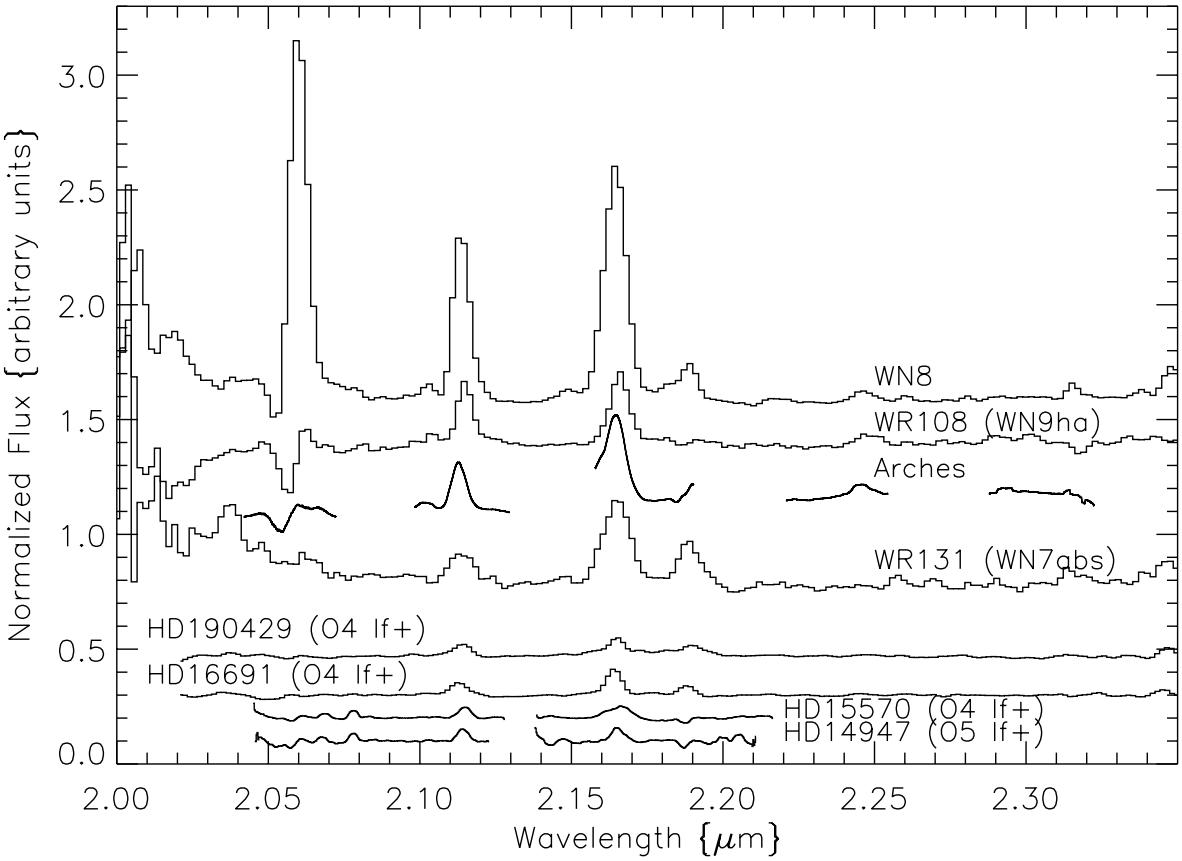

Fig. 6.— Comparison between average spectrum of Arches emission-line stars, spectra of representative WN7, WN8, and WN9 stars (Figer, McLean, & Najarro 1997), and spectra of individual O If$^+$ stars (Hanson et al. 1996). All spectra have been smoothed to match the resolution of the WR star spectra (R$\sim$525). Notice that the WNL and Arches stars have N III features in common at 2.104 μm and 2.25 μm. In addition, the equivalent-widths and relative ratios of equivalent-widths are similar in the WNL and Arches spectra. The spectra are all on the same scale, but shifted by a constant for presentation purposes.

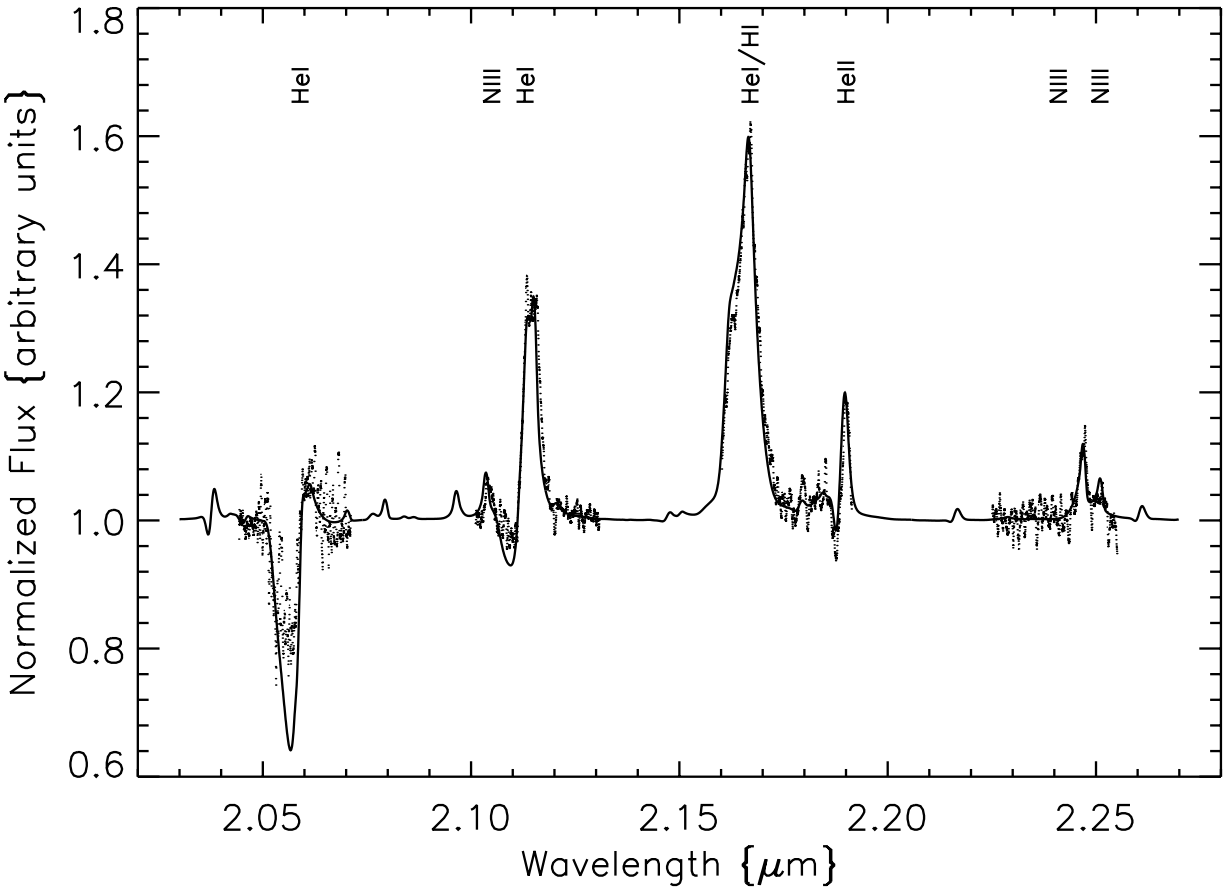

Fig. 7a.— Observed (*dots*) and modelled (*line*) spectrum of star #8.

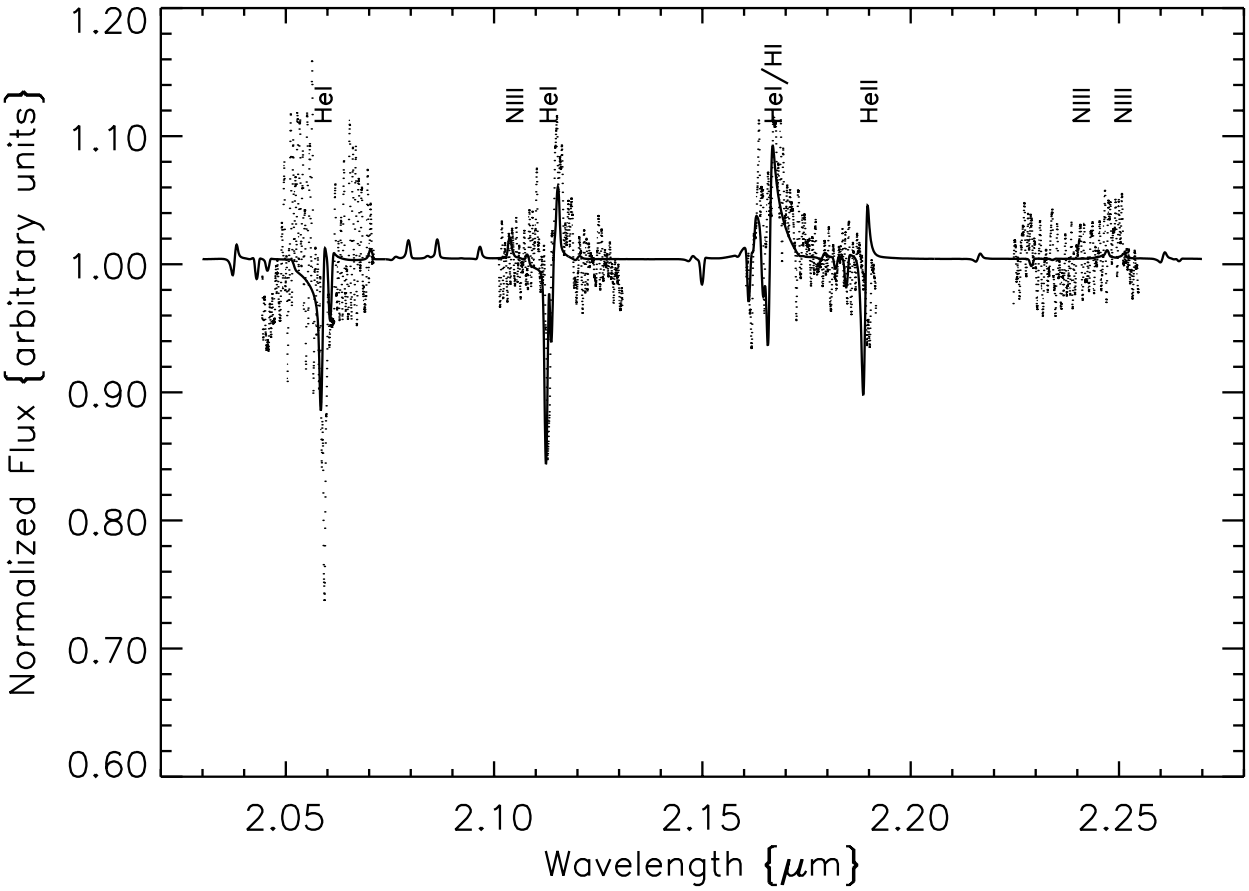

Fig. 7b.— Observed (*dots*) and modelled (*line*) spectrum of star #10.

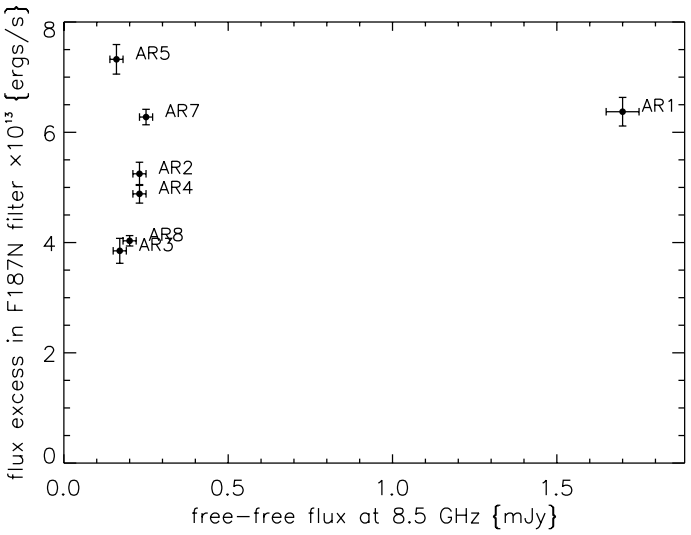

Fig. 8a.— Plot of $(F_{\rm F187N} - F_{\rm F190N}) \times \Delta\lambda$ versus $F_{8.5\ \rm GHz}$.

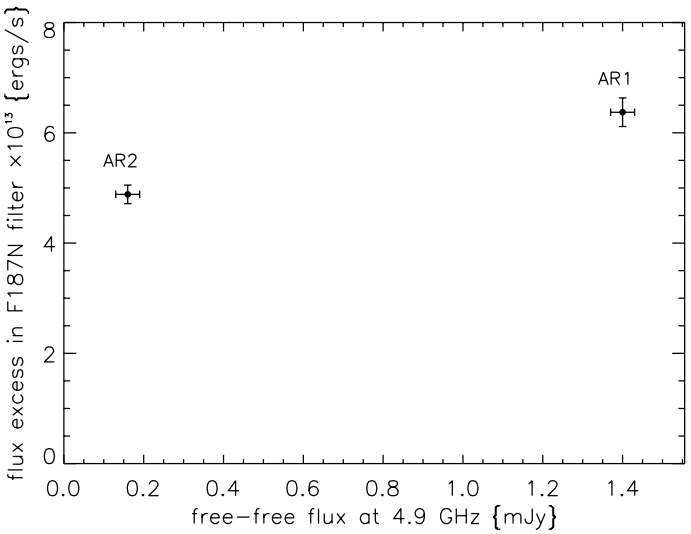

Fig. 8b.— Plot of $(F_{\rm F187N} - F_{\rm F190N}) \times \Delta\lambda$ versus $F_{4.9\ \rm GHz}$.

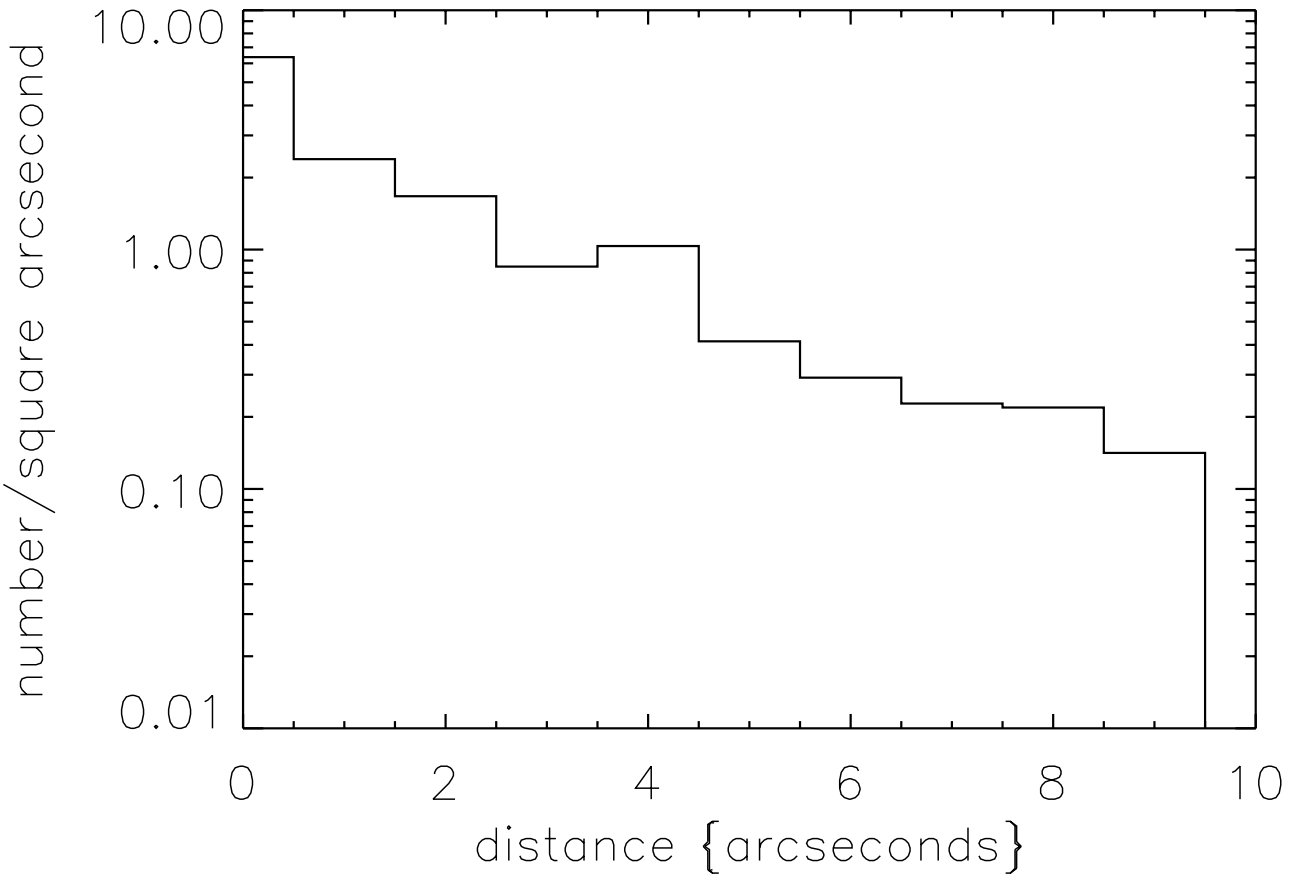

Fig. 9.— Histogram of massive star separations from cluster center. Data are taken from Table 3.